

THESIS

DEVELOPMENT OF A LIQUID ARGON PURITY MONITORING SYSTEM

Submitted by
Samuel J. Fogarty
Department of Physics

In partial fulfillment of the requirements
For the Degree of Master of Science
Colorado State University
Fort Collins, Colorado
Spring 2023

Master's Committee:

Advisor: John Harton

Michael Mooney
Carmen Menoni

Copyright by Samuel J. Fogarty 2023

All Rights Reserved

ABSTRACT

DEVELOPMENT OF A LIQUID ARGON PURITY MONITORING SYSTEM

Liquid argon time-projection chambers (LArTPCs) are used to detect charged particles and measure their properties. Charged particles that pass through the liquid argon (LAr) in a LArTPC ionize and excite argon atoms, producing ionization electrons and prompt scintillation light. The ionization electrons drift through the LAr volume in a uniform electric field and produce a signal at the anode. The scintillation light is used to determine the drift coordinate of an event, which allows for 3D reconstruction of tracks and interactions. Electro-negative impurities lead to the reduction of the ionization electrons and scintillation light. They worsen a detector's ability to perform event reconstruction by reducing the signal-to-noise ratios. A purity monitor is a device that is often used alongside LArTPCs to monitor the LAr purity. It extracts electrons from a photo-cathode via the photoelectric effect and drifts them through LAr to an anode using an electric field. When traversing the purity monitor, some of the electrons will be lost due to impurities along the way. As a result, the drift-electron lifetime, which is related to the LAr impurity concentration, can be determined by measuring the difference in charge between the cathode and anode. This method allows for continuous purity monitoring of the LAr used in a LArTPC. This thesis describes the development and testing of a purity monitoring system that is used in conjunction with a LArTPC at Colorado State University.

ACKNOWLEDGEMENTS

I want to thank my advisor, Dr. John Harton, for his support throughout this project and my first few years as a CSU graduate student. Working with him has been a joy since Day 1, and his advice and guidance have been a tremendous help in producing this work. This project has helped to develop my skills and knowledge of hardware, electronics, data analysis, coding, and optics. For this reason, I am very thankful for the opportunity to work on this project. I look forward to the opportunities that await me while I pursue my Ph.D.

I would be remiss not to acknowledge technical support on this project from people in the department. Jay Jablonski and Christian Norris supported this project through their work on setting up and operating the cryostat, pumps, and gauges used for the purity monitor, as well as teaching me how to operate parts of the apparatuses myself. They have also been a reliable and valuable source of advice and knowledge that has helped move this project forward. Jay was a crucial resource in the design phase of our purity monitor. In particular, he was instrumental in constructing numerous designs and models for this project that were all eventually realized. Machine Shop manager Jeff Breitschopf was instrumental in machining various components for this project, taught me valuable skills and techniques relating to machining, and taught me how to use multiple machine shop tools.

I am grateful for support from the US Department of Energy award DE-SC0017740, which has allowed me to work full-time on this project for over a year. I would also like to acknowledge support for this project, including a grant from the Dean's Faculty & Staff Success Program at CSU and a grant from the Graduate Student Council at CSU. These grants allowed us to make crucial upgrades to the apparatuses used in this project in various areas.

And, of course, I would like to thank my incredibly supportive and loving family for supporting me throughout my years at CSU and the over two decades leading up to now. I would not be here right now pursuing my dream without their continued and unwearying support.

TABLE OF CONTENTS

ABSTRACT	ii
ACKNOWLEDGEMENTS	iii
LIST OF TABLES	vi
LIST OF FIGURES	vii
Chapter 1 Introduction	1
1.1 LArTPCs and DUNE	1
1.1.1 Working Principle of LArTPCs	1
1.1.2 The DUNE Experiment	1
1.1.3 The Effect of Impurities in a LArTPC	2
1.1.4 The SingleCube Detector	3
1.2 Scintillation and Ionization in LAr	3
1.3 Electron Attachment in LAr	6
1.3.1 Formula Derivation	6
1.3.2 Effects of Specific Impurities	7
1.4 Measuring LAr Purity	8
1.4.1 Using LArTPC Data	8
1.4.2 Using a Purity Monitor	9
1.4.3 Working Principle of Purity Monitors	9
1.4.4 Research at CSU	11
Chapter 2 Electronics and Data Acquisition	12
2.1 Charge Amplifiers	12
2.1.1 Derivation	12
2.1.2 Electron Lifetime with Corrections	16
2.1.3 Input Current Reconstruction	17
2.1.4 PCB Designs	18
2.2 High Voltage Filters	19
2.3 Data Acquisition and Analysis	20
2.4 Grounding Scheme	21
Chapter 3 Light Production and Transmission	23
3.1 Xenon Flash Lamps	23
3.2 Optical Fibers	26
3.3 Lenses	27
Chapter 4 The Purity Monitor	30
4.1 Overview	30
4.2 Photo-cathodes	31
4.3 Cathode and Anode Grids	32
4.4 Electric Fields	35

4.5	Installation and Tests	36
Chapter 5	Purity Monitor Tests	40
5.1	Vacuum Performance	40
5.2	Initial Purity Monitor Tests in LAr	44
5.2.1	Experimental Setup and Tests	44
5.2.2	Factors Impacting Signal Size	45
5.3	Increasing Signal Size	47
5.3.1	Gold vs. Silver Signals	47
5.3.2	Xenon Flash Lamp Signals Comparison	49
5.3.3	Lenses Performance	51
5.4	Density Dependence of Signals in Gaseous Argon	54
5.5	LAr Tests with Upgraded Purity Monitor	56
5.5.1	Changes to the Purity Monitor Setup	56
5.5.2	Cathode Signals and Field Dependence	57
5.5.3	RC Correction for LAr Signals	58
5.5.4	Lessons Learned	61
5.5.5	Estimated Anode Signal Size	62
5.5.6	Next Steps	65
Chapter 6	Conclusion	66
Bibliography	67

LIST OF TABLES

3.1	Specifications of the xenon flash lamps used in this work.	25
4.1	Grid parameters, inefficiencies, and field ratios for the purity monitor grids. The field ratios are the calculated minimum required field ratios for the cathode and anode grids to maintain grid transparency.	34
4.2	Characteristics and measurements of the purity monitors for the tests described in this work.	35
5.1	Primary differences between testing each purity monitor design in LAr.	56

LIST OF FIGURES

1.1	A diagram visualizing the processes that occur after a charged particle interacts with Ar. The dotted arrow indicates there are intermediary steps omitted.	4
1.2	The first purity monitor we have tested (left) and the second purity monitor we have tested (right). They were designed and built at UT Arlington and Colorado State University, respectively. The anode is at the top and the cathode is at the bottom in each image.	9
2.1	A schematic of the HV filters and charge amplifiers.	12
2.2	Charge amplifier simulation showing the response to square pulses of current. $C = 1\text{pF}$ and $R = 100\text{M}\Omega$, but the same result is achieved using $C = 0.1\text{pF}$ and $R = 1000\text{M}\Omega$. . .	15
2.3	Diagram showing qualitatively what the cathode (left,blue) and anode (right,red) traces look like in LAr. The signal traces are shaped by the current pulse duration, the electron lifetime, and the RC time constants.	17
2.4	Top-down images of the through-hole charge amplifiers PCB (left) and the surface-mount charge amplifiers PCB (right).	18
2.5	The HV filters in an aluminum enclosure. They are enclosed within a plastic box to isolate all the input/output connections. SHV outputs (cathode, anode, and ground) are on the left and SHV inputs (cathode and anode HV) are on the right. BNC outputs for the cathode and anode currents are also on the right.	20
2.6	Demonstration of the ability of HV filters to smooth out high-frequency signals produced by a signal generator. The amplitudes of high-frequency signals are reduced by the filters, while low-frequency signals are much less affected. The trends do not appear to depend on the input voltage (at low voltages).	20
2.7	Purity monitor control and data acquisition station for testing the purity monitors in vacuum, gaseous argon, and LAr.	21
2.8	Schematic of various connections in the purity monitor system. The AC power cable also carries a ground connection.	22
3.1	UV spectra of the PAX-10 and Hamamatsu L7685 xenon flash lamps measured using an OceanOptics spectrometer (left), and the full Hamamatsu spectrum from the manufacturer (right). The threshold wavelengths for the different possible crystal structures for gold and silver are shown. The spectra of the two lamps are nearly the same shape and are offset from each other by a few nm.	23
3.2	The Hamamatsu L7685 xenon flash lamp (left) and the Excelitas PAX-1002-3 xenon flash lamp (right).	24
3.3	Two LA4052 plano-convex lenses simulated in the Zemax program on Sequential mode. The spot diagram on the right is the image of the source at a location optimized with the Spot Size Radial option.	27

3.4	The two mounts for the xenon flash lamp and optical fiber. The lens tube holder (left) allows the positioning of the lenses and optical fiber relative to the flash lamp. On the right is the setup that holds the end of the optical fiber close to the glass surface of the bulb.	28
3.5	Schematic of the lenses mounting apparatus with relevant distances.	29
4.1	Schematic of the CSU-designed purity monitor. Distances are approximate.	30
4.2	The cathodes and photo-cathodes for the first purity monitor (left) and the second purity monitor (right).	31
4.3	The grids for the CSU purity monitor. The first two images are from a Solidworks model and show how a mesh is placed between two rings. The third image is one of the completed grids.	32
4.4	A 2D cross-section equipotential field map of the CSU purity monitor made using the FreeFEM finite element software. The color scale is in volts and the distances are approximate. The cathode is at the bottom.	36
4.5	Purity monitor resistance test before cryostat insertion (left), full purity monitor apparatus and hanger (center), and top of purity monitor flange (right).	37
4.6	The cryostat lid when testing the first purity monitor (left) and when testing the second purity monitor (right).	38
4.7	Resistance and robustness test of the purity monitor resistors.	39
5.1	The setup used to test the purity monitors in a vacuum. This setup was moved and modified for tests in LAr.	40
5.2	Cathode and anode signals in a vacuum using the first purity monitor at 5×10^{-1} mbar. $V_C = -90V$ and $V_A = 500V$. The charge amplifier capacitance is assumed to be 5 pF when calculating the reconstructed current. The signals undergo a rolling average to smooth out the reconstructed current plot.	41
5.3	Cathode signal in a vacuum using the second purity monitor at 1.2×10^{-1} mbar. $V_C = -25V$ and $V_A = 450V$. The charge amplifier capacitance is assumed to be 1 pF when calculating the reconstructed current. The signals undergo a rolling average to smooth out the reconstructed current plot.	42
5.4	The cathode and anode signals observed in vacuum using the second purity monitor at 1.8×10^{-4} mbar with $V_C = -16V$ and $V_A = 300V$. The capacitances of the charge amplifiers are assumed to be 1 pF for calculating the reconstructed current.	43
5.5	Experimental setup for purity monitor LAr tests.	44
5.6	Cathode and anode signals in the second purity monitor for gold and silver. Yellow lines denote polynomial fits and black vertical lines denote the locations of the cathode peaks. $V_C = -50V$ and $V_A = 1000V$	47
5.7	Example of cathode signals in the second purity monitor for gold and silver. Yellow lines denote polynomial fits. $V_C = -50V$ and the anode power supply is turned off.	48
5.8	Purity monitor signals as a function of xenon flash lamp and photo-cathode. The optical fiber was positioned a few millimeters away from the surface of the bulb for each lamp. We used a noise trigger for both flash lamps. $V_C = -50V$ and $V_A = 1100V$	49

5.9	Cathode amplitude for both photo-cathodes as a function of lens position d in a vacuum. The amplitudes are normalized to the amplitude measured without lenses, which is indicated by a horizontal line at 1. The blue line represents 557.4 mV for gold and 8328 mV for silver.	52
5.10	Cathode amplitudes for both photo-cathodes as a function of lens position d ($V_C = -50V$). The amplitudes are normalized to the amplitude measured without lenses, which is indicated by a horizontal line at 1. The blue line represents 47.8 mV for gold and 528.9 mV for silver.	53
5.11	Cathode V_{peak} and t_2 are shown as a function of cryostat pressure. The silver photo-cathode is used in the second purity monitor for this test. $P = 12$ psi is approximately atmospheric pressure in Fort Collins, Colorado where this test took place. Each value is extracted from the average of 100 single traces with a polynomial fit.	54
5.12	Cathode signals observed with the second purity monitor in LAr. The signals have a timing resolution of $0.2\mu\text{s}$ and are smoothed with a rolling average using a 15 point window.	57
5.13	Cathode signal amplitude V_{peak} and peak time t_{peak} extracted from Figure 5.12 using the minimum data point after smoothing. Exponential fits are displayed in red with parameters shown.	58
5.14	Calculated charge from the cathode signals from Figure 5.13. Q_{leak} is calculated using the RC correction in equation 2.6.	59
5.15	Electron lifetime vs estimated anode V_{peak} for the CSU purity monitor (14.2 cm grid to grid distance). The plot on the right is a zoomed in version of the plot on the left. The anode-grid to anode resistance is $125M\Omega$	62
5.16	Electron lifetime vs estimated anode V_{peak} for the CSU purity monitor (4.39 cm grid to grid distance). The plot on the right is a zoomed in version of the plot on the left. The anode-grid to anode resistance is $150M\Omega$	64

Chapter 1

Introduction

1.1 LArTPCs and DUNE

1.1.1 Working Principle of LArTPCs

The liquid argon time-projection chamber (LArTPC) is a detector technology used by many experiments to measure the properties of charged particles. It is used to reconstruct the energies and 3D trajectories of charged particles in a volume of liquid argon (LAr). As charged particles traverse the medium, they lose energy by ionizing and exciting atoms. As a result, a trail of ionization electrons is produced along with scintillation light. The electrons drift through the detector in a uniform applied electric field and are detected at the anode plane. The charge measured at the anode can be used to calculate the charge deposited over unit length of a particle, $\frac{dQ}{dx}$, which can be used to determine the particle identity. It also provides information about the 2D trajectories of particles. Scintillation light from prompt electron-ion recombination is detected just nanoseconds after being created, providing an initial time t_0 for an ionization event. Comparing the detection time of scintillation light with the arrival time of charge at the anode, and folding in the known electron drift speed, enables the reconstruction of the drift coordinate of an event. Detection of scintillation light and drifted charge is used to reconstruct the 3D trajectories of particles in a LArTPC [1, 2]. The LArTPC technology is used by the Deep Underground Neutrino Experiment (DUNE) run by Fermilab [2].

1.1.2 The DUNE Experiment

The primary goal of the DUNE experiment is to detect neutrinos and measure their properties. The experiment will produce a strong source of neutrinos at Fermilab in Illinois. It will measure neutrino oscillations, a phenomenon where neutrinos spontaneously change between the three

types (electron, muon, and tau neutrinos).¹ To accomplish this, it will have a detector near the beam production point called the LAr near detector (ND-LAr) and a detector 800 miles (1300 km) away called the far detector. ND-LAr is meant to monitor the neutrinos before oscillations take place, while the far detector monitors the neutrinos after ample oscillations have occurred. However, since neutrinos are neutral particles, they do not produce ionization in a LArTPC. Instead, they produce charged particles when they interact in the detector. As a result, a LArTPC can only see the remnants of a neutrino interaction which are used to infer the properties of the incident neutrino.

DUNE has specific requirements on the reduction of ionization charge due to impurities in its LAr detectors. These requirements are set in order to allow the detectors to achieve their various goals. For example, ND-LAr requires that ionization charge is reduced by no more than 54% by the time it reaches the anode. This ensures that a certain level of signal-to-noise ratio (S/N) is maintained. A low S/N would make it challenging to see ionization signals over the noise of the electronics. To further improve the S/N, the detectors utilize cryogenic electronics to reduce electronic noise. LAr filters are often employed in LArTPCs to reduce the concentration of electro-negative impurities thereby increasing the electron lifetime and S/N.

1.1.3 The Effect of Impurities in a LArTPC

Each argon atom in a LArTPC has a full atomic shell and a very low chemical reactivity. As a result, electrons drifting in a LArTPC traverse the LAr without being captured by the medium itself. However, electro-negative impurities (*e.g.*, O₂, H₂O, and N₂) in LAr tend to attach to drifting electrons. These electrons are lost and the charge detected at the anode is reduced. Some potential sources of electro-negative impurities are the LAr liquification process, out-gassing from the detector materials, or leaks that expose the LAr to air. LArTPCs typically utilize oxygen getters and molecular sieves to remove oxygen and water impurities from LAr.

¹Multiple other experiments have studied or will study neutrino oscillations, including the MINOS and NOvA experiments ran by Fermilab, the Super-Kamiokande and Hyper-Kamiokande experiments in Japan, and the Sudbury Neutrino Observatory in Canada.

The electron attachment process is described, to a good approximation, by $e^{-t/\tau}$ where t is the total time an electron has drifted and τ is the electron lifetime. The electron lifetime is the average time that an electron drifts before it is captured by an impurity. The reduction of the drifted charge can be corrected for by multiplying the detected charge by $e^{t/\tau}$. The drift time is determined from the detection of prompt scintillation light. The electron lifetime can be extracted with a purity monitor or from the analysis of cosmic ray muon data.

1.1.4 The SingleCube Detector

A small-scale prototype of ND-LAr called SingleCube operates at Colorado State University. The detector is used to test new technologies and techniques for the DUNE experiment. The detector is a LArTPC in the form of a 30 cm cube contained within a cryostat. It consists of a negatively high-voltage biased cathode plane, a resistive field cage for field uniformity, a pixelated anode plane held at ground, and cryogenic electronics. The bias voltages of the cathode and anode produce an electric field pointing toward the cathode. Ionization electrons drift in the field and are collected on the pixels at the anode. The charge is not digitized until it exceeds a configurable threshold [3]. This was implemented to reduce the heat produced by the cryogenic electronics that can increase LAr boil-off. The detector utilizes filters to reduce the concentration of impurities in the LAr. The SingleCube detector will need to satisfy DUNE's S/N requirements in order to be able to test new technologies and techniques for DUNE.

1.2 Scintillation and Ionization in LAr

Two types of interactions lead to the production of free electrons and scintillation light. Each interaction results in the production of scintillation light peaked at 128 nm, while only one produces ionization electrons. The interactions are:

1. A charged particle directly excites an argon atom
2. A charged particle ionizes an argon atom, resulting in an electron-ion pair

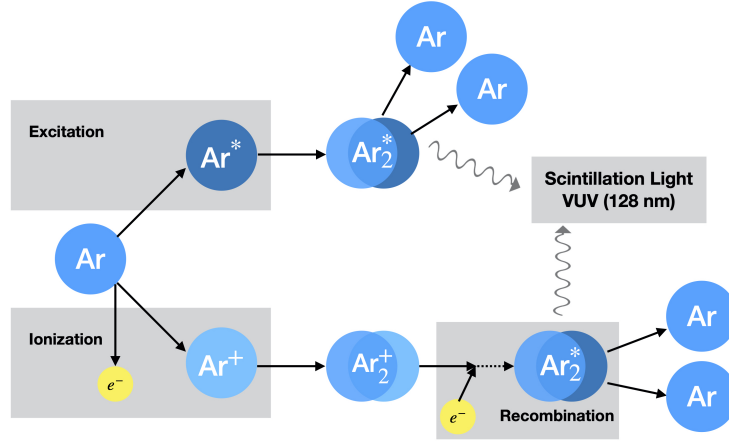


Figure 1.1: A diagram visualizing the processes that occur after a charged particle interacts with Ar. The dotted arrow indicates there are intermediary steps omitted.

Figure 1.1 visualizes the processes following each interaction. Both interactions produce the excited dimer (excimer) Ar_2^* which leads to the emission of scintillation light [4–6]. There are only a few processes following excitation. Ar_2^* is immediately produced:



Then it undergoes de-excitation [7, 8]:



γ denotes the scintillation light produced in this process, which is sharply peaked at about 128 nm [9].

The set of processes following ionization is longer than excitation. Firstly, a charged particle ionizes an Ar atom:

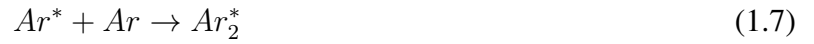


The energy required to produce an electron-ion pair is 23.6 eV on average [4]. Particles with less kinetic energy than 23.6 eV will not ionize an argon atom.

Next, a molecular ion is formed from an argon ion and a nearby argon atom



An ionization electron will likely combine with this molecular ion at zero applied electric field. A non-zero applied electric field increases the likelihood that the electron escapes before recombination occurs. If recombination occurs then Ar_2^* is produced, just like what follows ionization. The processes are



Like what follows excitation, Ar_2^* undergoes the de-excitation process producing two neutral argon atoms and a photon with a spectrum peaked at about 128 nm. At zero applied electric field, 57% of the scintillation light is a result of recombination and 43% is a result of excitation [6]. However, in the applied electric field within a LArTPC less recombination occurs.

The behavior of ionization charge and scintillation light in LAr as a function of the applied electric field was investigated by Kubota et al. [5]. They showed that as the applied electric field increases, the collected charge increases and the measured light intensity decreases. This behavior continued until they reached an electric field of about 8-10 kV/cm, where the collected charge and light intensity flattened as a function of the field. The leveling out of the collected charge indicates that almost no recombination takes place at a high field. If any did, we would continue to see an increase in collected charge with an increase in the field. If no recombination occurs at a high field and scintillation light is still observed, then scintillation light is being produced by other means such as argon excitation.

1.3 Electron Attachment in LAr

1.3.1 Formula Derivation

Electron attachment is a process where an electro-negative molecule, S , attaches to a drifting electron [10]:



The rate of the process depends on the particular molecule and its electro-negativity. Attachment may also impact scintillation light yield by preventing recombination and subsequent scintillation [8]. However, this effect is expected to be negligible since the attachment process is much slower than the formation of Ar_2^* .

Here we will denote concentration by n which implicitly depends on the time, t . The rate of change of the free electron concentration, n_e , produced by ionization events is described by the following differential equation [8]:

$$\frac{dn_e}{dt} = -k_e n_S n_e \quad (1.9)$$

The rate constant for attachment, k_e , depends on the molecule involved and has units of $\text{ppm}^{-1}\mu\text{s}^{-1}$. Concentration has units of ppm (parts-per-million). n_S is the concentration of impurities. We can solve equation 1.9 to find an equation for n_e . By rearranging, we can write

$$\frac{-1}{k_e n_S} dn_e = dt \quad (1.10)$$

Integrating and assuming that n_S is constant with respect to both time and n_e :

$$\frac{-1}{k_e n_S} \ln \left(\frac{n_e(t)}{n_e(t_0)} \right) = t - t_0 \quad (1.11)$$

Setting $t_0 = 0$, solving for $n_e(t)$, and replacing n_e with charge Q :

$$Q(t) = Q(0)e^{-t/\tau} \quad (1.12)$$

where $\tau \equiv \frac{1}{k_e n_S}$ is the electron lifetime. Equation 1.12 describes how much charge is lost due to impurities over a period of time, t , and at a specific electron lifetime. The number of free electrons decreases exponentially as a function of drift time. By multiplying a measured amount of charge in a TPC by $e^{t/\tau}$, we recover how much charge was initially drifted from an ionization event. Then by multiplying by the appropriate recombination factor, we would recover the total ionization charge produced in the ionization event. We will discuss some important corrections that need to be made to equation 1.12 in order to use it with purity monitors.

1.3.2 Effects of Specific Impurities

Specific impurities such as oxygen, nitrogen, water, and carbon dioxide are known to attach to free electrons in LAr. Biller et al. [11] determined that at 500 V/cm, the drift electron attenuation length (analogous to electron lifetime) decreased with increasing O₂ concentration from 1 to 7 ppb. This showed experimentally that there is a strong correlation between O₂ concentration and electron lifetime. Hofmann et al. [12] also confirmed this strong correlation when they observed that with an increase of O₂ concentration comes a dramatic decrease in electron lifetime from 1 to 60 ppm.

Nitrogen also participates in attachment [11, 12]. Biller et al. showed that N₂ and O₂ have the same impact on electron lifetime *only* when the N₂ concentration is 1000 times larger than the O₂ concentration. This means that the rate constant for attachment to O₂ is much larger than for N₂. Hofmann et al. found that even when the N₂ concentration was 30 times larger than the O₂ concentration, the effect of N₂ was minor and the effect of O₂ was strong. We conclude that N₂ has a small impact on drifting electrons in LArTPCs, while O₂ has a strong impact. Ref [13] lists attachment rate constants for multiple different impurities.

At zero field, they found:

1. $k_{\text{O}_2} = 4.1_{-0.9}^{+1.5} \text{ ms}^{-1}\text{ppb}^{-1}$
2. $k_{\text{CO}_2} = 0.175 \pm 0.018 \text{ ms}^{-1}\text{ppb}^{-1}$
3. $k_{\text{H}_2\text{O}} = 0.093_{-0.033}^{+0.028} \text{ ms}^{-1}\text{ppb}^{-1}$

The attachment rate constant for O_2 is over 30 times larger than for H_2O and over 20 times larger than for CO_2 at zero field. The rate constants may be different at a higher electric field, such as 500 V/cm in a LArTPC. At 500 V/cm, we find that $k_{\text{O}_2} = 3.075_{-1.475}^{+2.749} \text{ ms}^{-1}\text{ppb}^{-1}$ by using a conversion factor in Ref [13]. Plugging $n_{\text{O}_2} = 1 \text{ ms}$ into $\tau = \frac{1}{k_e n_{\text{O}_2}}$ and assuming O_2 is the only impurity, we find that n_{O_2} must be less than about 250 ppt to get an electron lifetime of more than 1 ms.

1.4 Measuring LAr Purity

1.4.1 Using LArTPC Data

Data collected by LArTPCs of minimum-ionizing muons from cosmic rays can be used to measure the electron lifetime in LAr. When these muons cross the drift length in a TPC, one can create a plot of drift time, t_{drift} , versus charge deposited per unit length, $\frac{dQ}{dx}$, for muon track segments. By performing a fit to this plot with the derivative of equation 1.12 with respect to drift length, x , one can extract the electron lifetime. One downside to this method is that it requires the TPC to be completely covered by LAr, meaning that the purity can only be known after the detector has started operations. Low LAr purity can lead to a failed test of the detector by substantially reducing the number of ionization events that can be observed. It is therefore a substantial risk to only have the capability to measure purity once the detector starts running, since at that point it may be too late to fix the problem of low purity LAr. That is, unless the LAr can be recirculated through the filters and purified more after a LAr fill is completed.

1.4.2 Using a Purity Monitor

A purity monitor is a device that measures electron lifetime in LAr and can be operated independently from the detector. It is typically smaller than the TPC it is used alongside, so it does not require as much LAr to submerge it completely. It is useful to use a purity monitor to measure LAr purity while or before filling the detector. It could be used to detect changes in electron lifetime which, for example, might be caused by leaks in the cryogenic infrastructure. Another use is in conjunction with a detector placed deep underground such as the DUNE far detector. In such a case, cosmic ray muons would be sparse due to the substantial rock overburden and therefore could not be used to measure electron lifetime with the method described above.

1.4.3 Working Principle of Purity Monitors

The two purity monitor designs that we have tested are shown in Figure 1.2.

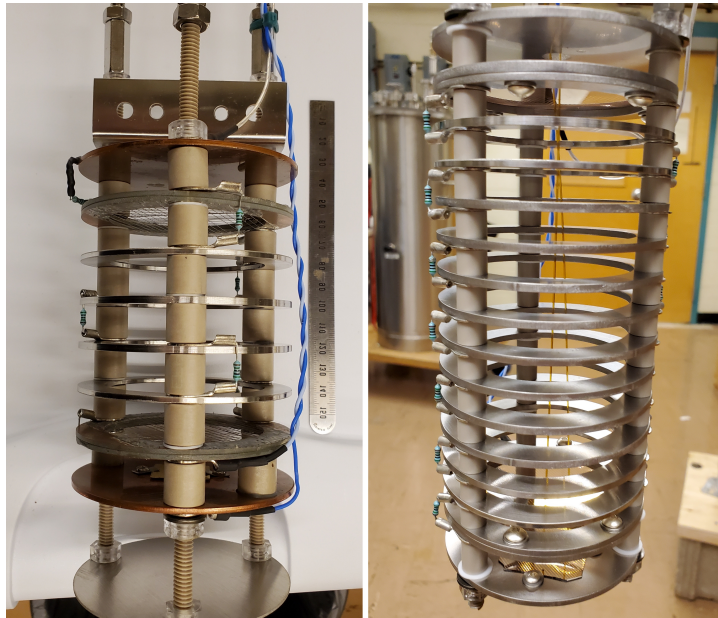


Figure 1.2: The first purity monitor we have tested (left) and the second purity monitor we have tested (right). They were designed and built at UT Arlington and Colorado State University, respectively. The anode is at the top and the cathode is at the bottom in each image.

Their designs are largely based on the original pioneering work by the ICARUS collaboration [14] with some modifications.

The purity monitor design shown on the left in Figure 1.2 was the first design we tested in vacuum and LAr. Our design (shown on the right) was informed by the various tests we performed with the first design. Note that once our purity monitor design was built, the first purity monitor was decommissioned and dismantled. The purity monitors drift electrons vertically in a uniform electric field through LAr. Electrons are produced at the cathode using the photo-electric effect. Ultraviolet light impinges on a photo-cathode and ejects electrons from the material. The light is produced by an external xenon flash lamp and transmitted to the photo-cathode via quartz optical fibers. The photo-electrons then drift a certain distance until they are collected at the anode. The corresponding currents from the cathode and anode pass through charge amplifiers outside the LAr to produce a voltage nominally proportional to the input charge, Q , where $Q \approx C(V_{\max} - V_0)$. C is the capacitance of the charge amplifier, V_{\max} is the maximum voltage, and V_0 is the baseline voltage. Wire grids are placed on either end of the purity monitor to shield the cathode and anode from induced current caused by the drifting charges. The electric fields are produced by biasing the anode and cathode with DC voltages. There is a series of stainless steel rings between the anode and cathode. They are connected to each other, the cathode and anode grids, and the anode by resistors. This creates a voltage divider that helps to maintain the uniformity of the electric field.

The charge measured at the anode, Q_A , will be smaller than the charge measured at the cathode, Q_C , due to attachment by impurities. The ratio Q_A/Q_C can be used to calculate electron lifetime. The following equation describes drift electron attenuation in a purity monitor as a function of electron lifetime, and is a rearrangement of equation 1.12:

$$\tau = \frac{-t_{\text{drift}}}{\ln(Q_A/Q_C)} \quad (1.13)$$

In Chapter 2, we discuss corrections to equation 1.13 that need to be taken into account for purity monitors.

1.4.4 Research at CSU

This thesis will describe work done to develop and test a LAr purity monitoring system to accompany the SingleCube detector at CSU. Initial tests were performed with a purity monitor developed at UT Arlington based on the design in Ref. [15]. Subsequent tests were performed with a purity monitor developed at CSU largely based on the designs in Refs. [15, 16]. Multiple changes to the system were tested to increase the S/N of the purity monitor signals, including using a more powerful xenon flash lamp, improving UV transmission to the photo-cathode, and replacing the gold photo-cathode with a silver one. We will discuss various tests of the purity monitors in a vacuum, gaseous argon (GAr), and LAr.

Chapter 2

Electronics and Data Acquisition

2.1 Charge Amplifiers

2.1.1 Derivation

We use charge amplifiers to measure the currents from the cathode and anode in the purity monitors. A charge amplifier acts as a current integrator and produces an output voltage nominally proportional to the integrated input current. The circuit has an RC feedback loop in parallel with an operational amplifier (op-amp). A circuit diagram is shown in Figure 2.1. The op-amp keeps a zero potential difference between its two inputs. The “-” terminal is the inverting input and the “+” terminal is the non-inverting input. The non-inverting input is always connected to ground in our application, which sets the inverting input to a virtual ground. A signal from the purity monitor is connected to the inverting input. No current flows into the inverting input.

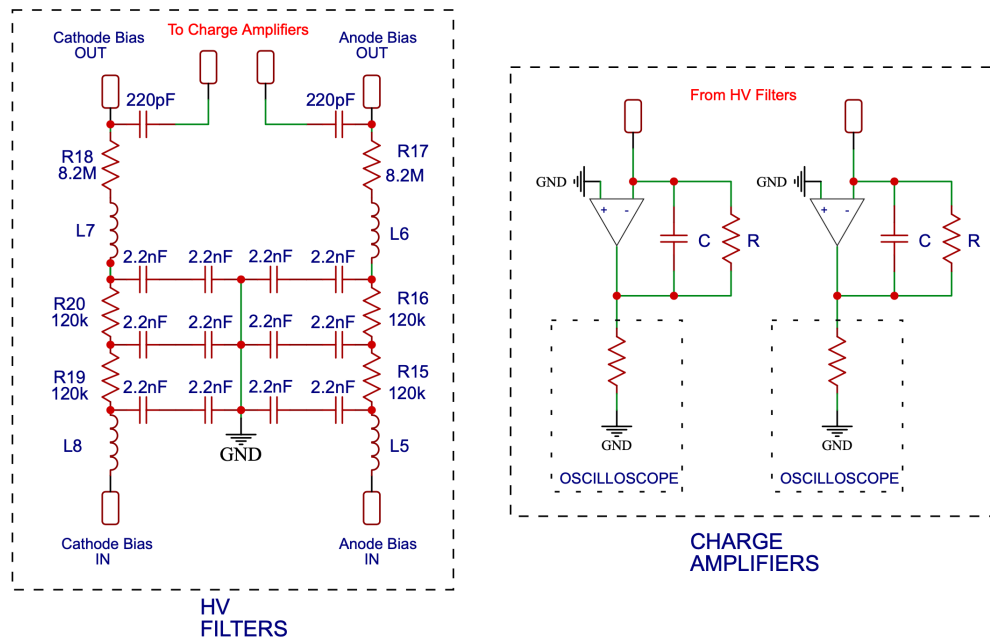


Figure 2.1: A schematic of the HV filters and charge amplifiers.

An input current, I_{in} , from either the cathode or anode passes through the resistor and capacitor in a charge amplifier. The current then passes through a $1\text{M}\Omega$ resistor to ground in the oscilloscope. We also include a 50Ω terminator for each signal at the input of the oscilloscope. The current can be written as

$$\begin{aligned} I_{\text{in}}(t) &= I_{\text{R}}(t) + I_{\text{C}}(t) \\ &= \frac{V(t)}{R} + C \frac{dV(t)}{dt} \end{aligned} \quad (2.1)$$

$I_{\text{R}}(t)$ and $I_{\text{C}}(t)$ are the currents through the resistor and capacitor, respectively. The currents and voltages in equation 2.1 and elsewhere in this chapter are dependant on the time t , unless otherwise stated. The voltage drop across the resistor and capacitor is the same due to Kirchhoff's loop rule. And since the inverting input is held at 0V , the voltage drop across the resistor and capacitor is equal to the output voltage of the circuit, $V(t)$. The integral of the input current over the pulse duration, Δt , is equal to the total charge, Q :

$$Q = \int_{t_i}^{t_f} I_{\text{in}}(t) dt \quad (2.2)$$

Integrating equation 2.1 with respect to time yields

$$Q = \frac{1}{R} \int_{t_i}^{t_f} V(t) dt + C(V_{\text{max}} - V_0) \quad (2.3)$$

where t_i and t_f are the initial and final time of the current pulse respectively, $V_{\text{max}} \equiv V(t_f)$ is the maximum voltage, and $V_0 \equiv V(t_i)$ is the baseline voltage. Equation 2.3 can be used to calculate Q given the voltage output $V(t)$ of the charge amplifier. Note that Q should not be confused with the total charge extracted from the cathode, Q_0 . Q is the charge we get from integrating the input current, but Q_0 corresponds to the photo-electrons that leave the cathode and begin to drift to the anode. While the integral in equation 2.3 can be determined numerically, we choose R to be large to make it small. We make $RC = 100\mu\text{s}$ in our setup by using $C = 1\text{pF}$ and $R = 100\text{M}\Omega$.

In the case of a negligible integral, equation 2.3 reduces to

$$Q \approx C(V_{\max} - V_0) \quad (2.4)$$

By dividing by C , we see that the gain of the circuit is approximately $1/C$. The resistor leakage effect lowers $V(t)$ which lowers the S/N. Since the S/N decreases, the systematic error increases if we use equation 2.4 to calculate Q . We can calculate Q more accurately by using a correction:

$$Q = CV_{\text{peak}}f(\Delta t, RC) \quad (2.5)$$

where $V_{\text{peak}} \equiv V_{\max} - V_0$ and Δt is time between the start of the pulse and the peak. The function f is the RC correction factor that is derived in Ref. [16]. It depends on the RC constant of the charge amplifier and the time since the start of the pulse:

$$f(t, RC) = \frac{t/RC}{1 - e^{-t/RC}} \quad (2.6)$$

This correction is important in a purity monitor because the duration of each input current pulse to the charge amplifier depends on the electric field. For the cathode, the pulse duration can last as long as it takes for the electrons to drift from the cathode to the cathode-grid. The electrons induce a current on the cathode until they pass the cathode-grid. The cathode does not experience any induced current from charges beyond the grid, due to the shielding property of the grid. And for the anode, the pulse duration can last as long as it takes for the electrons to drift from the anode-grid to the anode. The electrons induce a current on the anode only once they pass the anode-grid. Over these pulse durations, the charge amplifier leads to a charge depletion by leaking charge through R or by discharging before all the charge has passed from cathode to cathode-grid or anode-grid to anode. Equation 2.6 corrects for these effects and can be used to recover the “true” charge.

Figure 2.2 shows the correction factor used on an EasyEDA simulation of charge amplifier responses to square pulses of varying width and constant integral. $Q_{\text{peak}} = CV_{\text{peak}}$ and Q_{leak} is calculated with a numerical integral of $V(t)/R$. We see in the figure that the total charge stored on the capacitor decreases as the pulse width increases. The total charge that flows through the resistor, Q_{leak} , increases as the pulse width increases. Adding Q_{leak} to Q_{peak} recovers Q . In addition, Q is recovered by multiplying CV_{peak} by the correction factor, like in equation 2.5. Therefore, we conclude that the correction factor can be used as a stand-in for the integral of $V(t)$ to correct for the charge amplifier charge depletion effect.

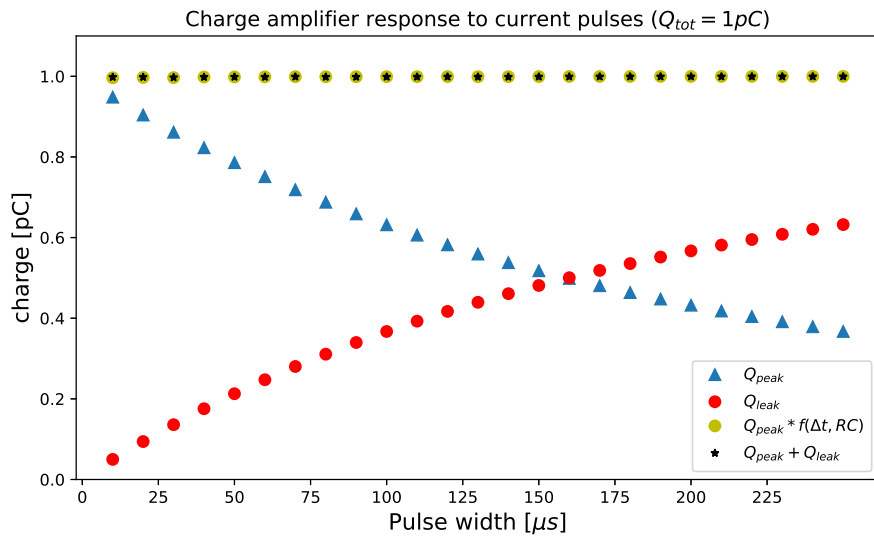


Figure 2.2: Charge amplifier simulation showing the response to square pulses of current. $C = 1\text{pF}$ and $R = 100\text{M}\Omega$, but the same result is achieved using $C = 0.1\text{pF}$ and $R = 1000\text{M}\Omega$.

2.1.2 Electron Lifetime with Corrections

By modifying equation 1.13, the electron lifetime with corrections can be calculated with the following equation [16]:

$$\tau \approx \frac{-1}{\ln(Q_A/Q_C)} \left(t_2 + \frac{t_1 + t_3}{2} \right) \quad (2.7)$$

where

$$Q_A/Q_C = \frac{g_C V_{\text{peak}}^a f(t_3, R_A C_A)}{g_A V_{\text{peak}}^c f(t_1, R_C C_C)} \quad (2.8)$$

In equation 2.7, t_1 is the time it takes for electrons to drift from the cathode to the cathode-grid, t_2 is the time it takes for electrons to drift from the cathode-grid to the anode-grid, and t_3 is the time it takes for electrons to drift from the anode-grid to the anode (see Figure 2.3). The gain ratio of the two charge amplifiers is $g_C/g_A = C_A/C_C$. We measure the gain ratio in a vacuum by measuring the same cathode signal in both charge amplifiers and calculating the ratio of the two values of V_{peak} . For one of our surface-mount PCB charge amplifier boards, this ratio was $g_C/g_A = 0.943$.

Equation 2.7 was derived in Ref. [16] by integrating the current from the cathode to the cathode-grid for the cathode signal, and from the anode-grid to the anode for the anode signal. It takes into account that the cathode and anode currents are an exponentially decreasing function of t and τ . This is reasonable because some electrons will be lost to impurities before they cross the cathode-grid and before they reach the anode, hence decreasing the induced current they produce. Equation 2.7 is true by assuming that $t_{1,3} \ll 2\tau$. It is not true when the lifetime is sufficiently low such that it is comparable to or less than $t_{1,3}$. In that case, a less simplified form of equation 2.7 can be found in Ref. [16] that can be used to calculate the electron lifetime:

$$\frac{Q_A}{Q_C} = \frac{t_1 \sinh(t_3/2\tau)}{t_3 \sinh(t_1/2\tau)} \exp\left(-\frac{\frac{t_1+t_3}{2} + t_2}{\tau}\right) \quad (2.9)$$

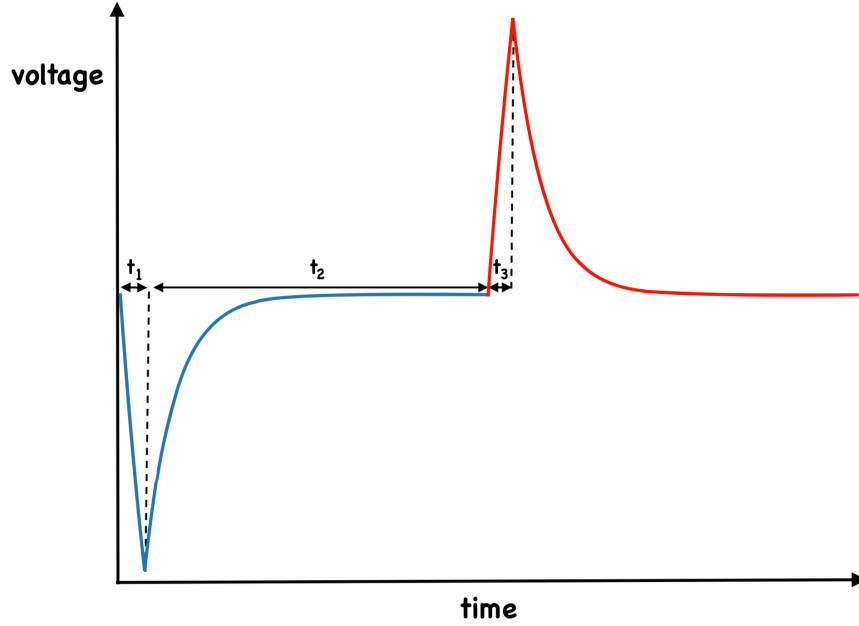


Figure 2.3: Diagram showing qualitatively what the cathode (left,blue) and anode (right,red) traces look like in LAr. The signal traces are shaped by the current pulse duration, the electron lifetime, and the RC time constants.

In this case, Q_A/Q_C is found using equation 2.8 and $t_{1,2,3}$ are extracted from the cathode and anode traces. To extract the lifetime, we can plot both sides as a function of τ and look for where they cross each other.

2.1.3 Input Current Reconstruction

From equation 2.1, where j is the index of a data point, we can write

$$I_{\text{in}}^j = \frac{V^j}{R} + C \left(\frac{V^{j+1} - V^j}{t^{j+1} - t^j} \right) \quad (2.10)$$

Equation 2.10 can be used to reconstruct the input current from the output voltage of a charge amplifier by numerically iterating through the data points. In a time series data set, t^j is the time and V^j is the voltage at index j . The numerical derivative sometimes leads to noisy reconstructed current in real data since noise causes large jumps in voltage from one point to the next. Performing the iteration on data smoothed with a rolling average or on a fit to the data helps reveal the structure

of the input current. We have found that this current reconstruction method works well for various pulse shapes in simulation (EasyEDA). The technique is demonstrated on real data in Chapter 5.

2.1.4 PCB Designs

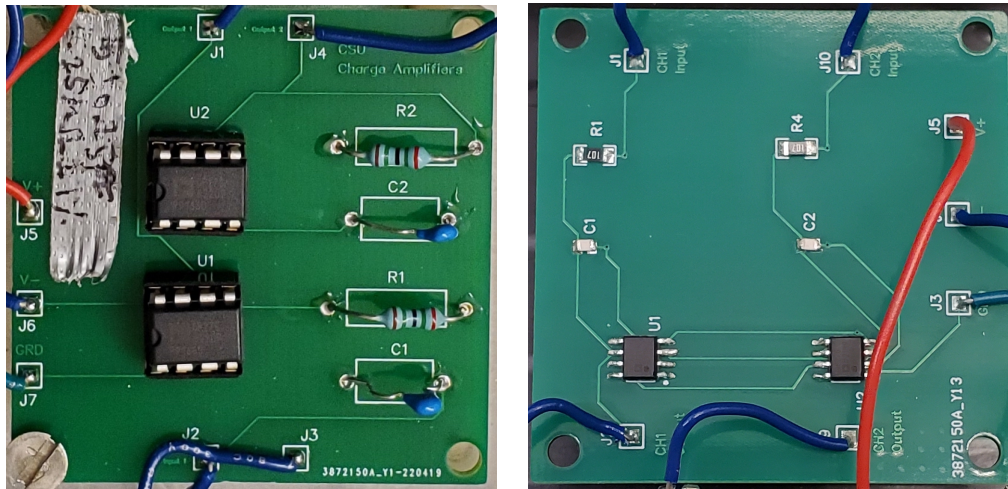


Figure 2.4: Top-down images of the through-hole charge amplifiers PCB (left) and the surface-mount charge amplifiers PCB (right).

We initially used a breadboard with two charge amplifiers soldered in for purity monitor tests. It used 5pF capacitors, 25M Ω resistors, and OP27G op-amps biased with $\pm 12V$. The board was beneficial for initial tests and exploration of charge amplifier output. One of the things we aimed to improve about the charge amplifiers was the amount of cross-talk between the two channels. Cross-talk is not a substantial issue when testing in LAr since the cathode and anode pulses would typically be separated by hundreds of microseconds. However, it could present an issue when using a very short drift length or high fields where the cathode and anode signals would overlap in time. Cross-talk can also distort signals observed in vacuum and gaseous argon since the signals overlap in time for our purity monitors. We also aimed to minimize parasitic capacitance to maximize the gain of the circuit. Parasitic capacitance is extra capacitance introduced in a circuit due to electrode proximity. It increases the feedback capacitance and lowers the gain of the circuit. The two PCB designs used in our purity monitor tests are shown in Figure 2.4. The through-hole board uses 5pF

capacitors, $25\text{M}\Omega$ resistors, and OP27G op-amps. The surface-mount board uses 0.1 pF capacitors, $100\text{M}\Omega$ resistors, and OP27GSZ op-amps. Upon inspection, we determined the total capacitance of each charge amplifier in the surface-mount board was about 1 pF , which makes the RC time constant about $100\mu\text{s}$. Both boards shown in Figure 2.4 have been used for purity monitor tests described in this work. The surface-mount board was used for tests of our purity monitor design in LAr, and it (or a future iteration) will be used for future purity monitor tests.

2.2 High Voltage Filters

In our setup, the bias voltages for the cathode and anode are filtered using high voltage (HV) filters. The filters remove spikes, surges, and noise that may be present in the HV signals. They are made of passive low-pass and high-pass filters comprising a combination of resistors, capacitors, and inductors. A schematic of the HV filters is shown in Figure 2.1. The HV filters used in our setup are shown in their enclosure in Figure 2.5. A 220 pF blocking capacitor between each HV filter and its corresponding charge amplifier blocks the HV signal. The current signals from the anode and cathode flow through the blocking capacitor to the charge amplifier. We show in Figure 2.6 that the HV filters smooth out square pulses at low pulse width and sine waves at high frequency by reducing the amplitudes of the signals. Low-frequency signals are much less affected by the filters. The filters will therefore output a smoothed HV signal.

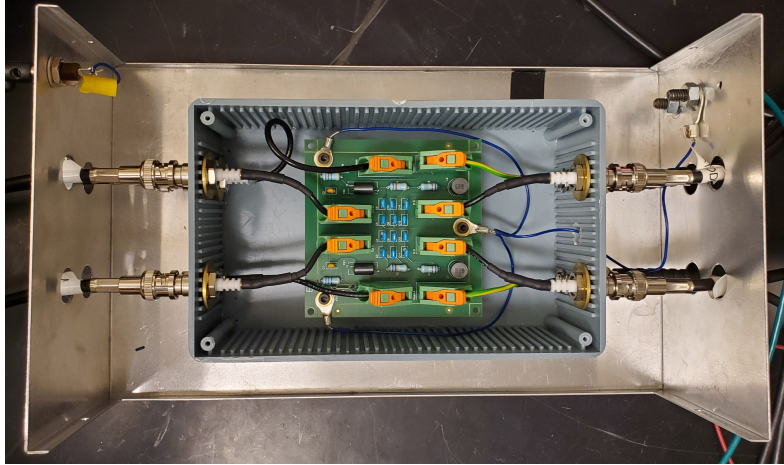


Figure 2.5: The HV filters in an aluminum enclosure. They are enclosed within a plastic box to isolate all the input/output connections. SHV outputs (cathode, anode, and ground) are on the left and SHV inputs (cathode and anode HV) are on the right. BNC outputs for the cathode and anode currents are also on the right.

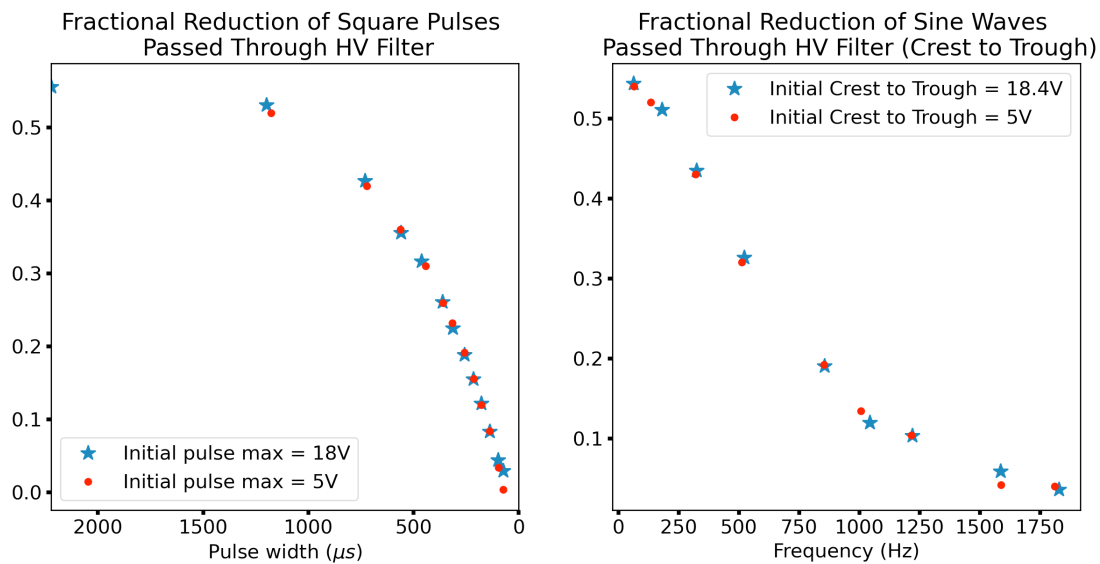


Figure 2.6: Demonstration of the ability of HV filters to smooth out high-frequency signals produced by a signal generator. The amplitudes of high-frequency signals are reduced by the filters, while low-frequency signals are much less affected. The trends do not appear to depend on the input voltage (at low voltages).

2.3 Data Acquisition and Analysis

We acquire the cathode and anode signals in an oscilloscope. The signal acquisition, when testing the first purity monitor design, was triggered by a TTL signal from the pulse generator that triggered the xenon flash lamp. The pulse generator triggered the xenon flash lamp at an adjustable rate of $<10\text{Hz}$. When testing our purity monitor design with a different xenon flash lamp, we were

unable to use this method of triggering the signal acquisition. So instead, we triggered the signal acquisition in the oscilloscope using the electromagnetic interference produced by the xenon flash lamp. The signals are averaged in the oscilloscope and saved to a USB flash drive for offline analysis in python. Alternatively, single traces are saved and averaged offline. The data acquisition and electronics setup are shown in Figure 2.7. In the analysis software, the first step is to subtract the average of the data points preceding the signal to account for the baseline voltage. We have tried a few methods for extracting the peak voltages and peak times in the analysis software. One method is to do a polynomial fit to a trace and then find the peak voltage of the fit. Another method is to first do a rolling average of the trace then find the peak voltage by finding the maximum or minimum data points. The former method is used predominantly in this work, but both methods have worked well. Analysis of simulated data verified that the fit performs well to extract the true mean and standard deviation in the presence of baseline noise and V_{peak} fluctuations.



Figure 2.7: Purity monitor control and data acquisition station for testing the purity monitors in vacuum, gaseous argon, and LAr.

2.4 Grounding Scheme

The grounding scheme and various connections for purity monitor testing are shown in Figure 2.8. The connections are designed to eliminate ground loops that could introduce noise to the system. Figure 2.8 specifically represents the setup when testing our purity monitor design, where the isolated power and ground is used, and the xenon flash lamp is isolated from the rest of the system

to reduce noise in the measurements. The isolated system is our detector power and ground that is a Fermilab-designed system that produces a low-noise power and ground for detector operations. When testing the first purity monitor design, the xenon flash lamp was not isolated and building power and ground were used.

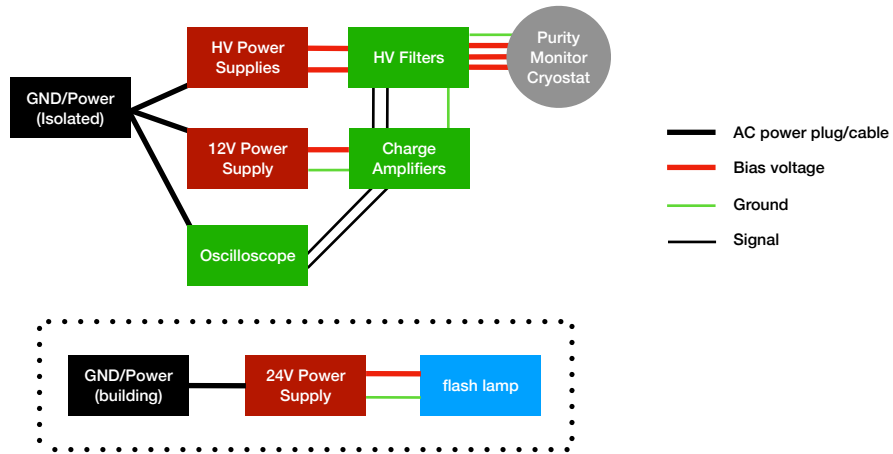


Figure 2.8: Schematic of various connections in the purity monitor system. The AC power cable also carries a ground connection.

Chapter 3

Light Production and Transmission

3.1 Xenon Flash Lamps

We use a xenon flash lamp to produce UV light needed to extract electrons from photo-cathodes. A xenon flash lamp has a xenon-filled bulb in parallel with a capacitor. Since xenon gas is an insulating medium, the gap between its two conductive electrodes has a high impedance that strongly resists the flow of current across it. When a trigger signal is applied to the lamp, the xenon atoms are ionized and an electrically conductive channel is created across the gap. The capacitor charges up to a high voltage and then discharges across the gap. The flow of current across the gap produces light with a wide spectrum. Figure 3.1 shows the spectra of the two xenon flash lamps that we have used for purity monitor testing.

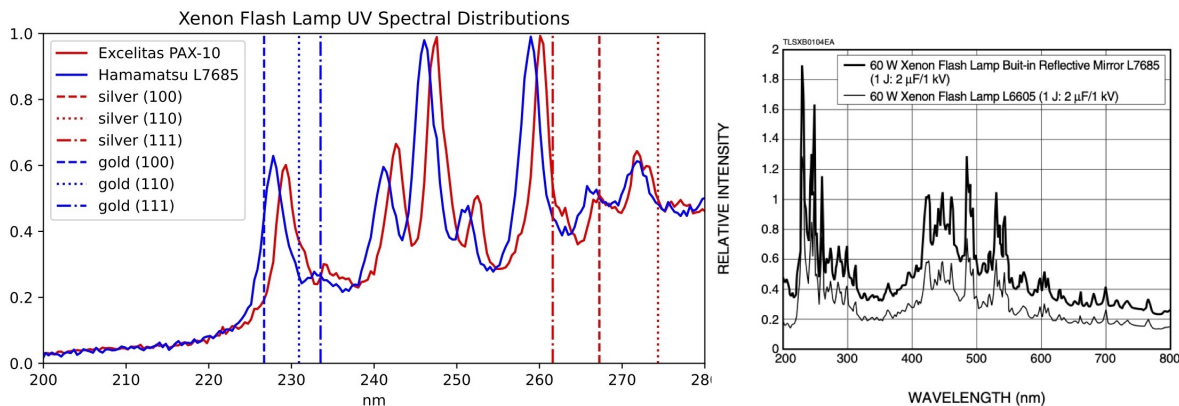


Figure 3.1: UV spectra of the PAX-10 and Hamamatsu L7685 xenon flash lamps measured using an OceanOptics spectrometer (left), and the full Hamamatsu spectrum from the manufacturer (right). The threshold wavelengths for the different possible crystal structures for gold and silver are shown. The spectra of the two lamps are nearly the same shape and are offset from each other by a few nm.

Gold and silver photo-cathodes only use a small portion of the spectrum because they have threshold wavelengths in the UV. In the left plot of Figure 3.1, any light with a wavelength below a threshold (denoted by a vertical line) can eject an electron. The three possible silver threshold

wavelengths, depending on crystal structure, are higher than the thresholds for gold. This means that silver can use 4-6 more of the UV peaks present in the spectrum to eject electrons. Because of this, we expect that silver will produce larger signals in a purity monitor than gold. We expect silver to prevail over gold since previous research [16] showed that silver produces about 3 times larger signals than gold in a purity monitor immersed in LAr. In Chapter 5, we describe tests we performed of gold and silver photo-cathodes in a purity monitor.



Figure 3.2: The Hamamatsu L7685 xenon flash lamp (left) and the Excelitas PAX-1002-3 xenon flash lamp (right).

The two xenon flash lamps we have used for purity monitor testing are shown in Figure 3.2. The xenon flash lamp we used when testing the first purity monitor design is the PAX-1002-3 from Excelitas [17]. To increase the light intensity, we replaced it with the Hamamatsu L7685 which is also used in Ref. [16]. The Hamamatsu L7685 is the flash lamp we have used to test our purity monitor design. The Excelitas lamp has the bulb, trigger, and power supply integrated into a single enclosure. The Hamamatsu L7685 includes a cooling jacket (E6611) which houses the xenon bulb and trigger socket, a power supply (C14352), and an external discharge capacitor (E7289-02). The bulb and power supply are cooled with built-in fans. Figure 5.8 in Chapter 5 compares the capabilities of the two flash lamps in a purity monitor. The specifications of the two xenon flash lamps are shown in Table 3.1.

Table 3.1: Specifications of the xenon flash lamps used in this work.

Model	Max. Discharge Voltage (V)	Discharge Capacitance (μ F)	Max. Avg. Energy per Flash (mJ)	Max. Avg. Power (W)
PAX-1002-3	1000	0.22	110	10
L7685	1000	2.1	1000	60

The inputs and outputs of the flash lamps use 9-pin D-sub connectors. To provide the input power and trigger signals through BNC cables, we use a grounded interface box that couples the D-sub connectors with panel-mount BNC connectors via wires. The input power is provided by the B&K Precision 1788, a single output DC power supply. In particular, +12 VDC and +24 VDC is provided for the Excelitas and Hamamatsu lamps, respectively (3-4 amps at peak). The trigger is a voltage pulse provided by a function generator with 5V amplitude and greater than 10 μ s pulse width. Alternatively, the lamps can be triggered internally which does not require a function generator. The total energy per flash is $E = \frac{1}{2}CV^2$, where V is the maximum voltage across the capacitor and C is the capacitance. Since E is linear in C , we see that the larger capacitance of the Hamamatsu lamp makes it emit much more energy than the Excelitas lamp by about a factor of 10. The Hamamatsu lamp ground, power supply, and pulse generator are connected to building power and ground, while the rest of the purity monitor system uses detector power and ground. This electrically isolates the flash lamp from the rest of the system. This is done to minimize the flash lamp induced noise on the signals in the oscilloscope. When using the Excelitas lamp, this kind of isolation is not used.

To stabilize the output of the Hamamatsu flash lamp, we run it for about 20 minutes prior to any tests. We chose this amount of time because the purity monitor signals would reach a stable size after about 15-20 minutes of running the flash lamp. The manufacturer also recommends allowing the flash lamp to warm up to allow it to stabilize.

3.2 Optical Fibers

We use multi-mode optical fibers to transfer light from the xenon flash lamp to the purity monitor photo-cathodes. Optical fibers are made of silica glass and utilize total internal reflection to confine and guide light within the fiber. We use multi-mode fibers because they have a large number of paths (modes) for light to traverse the length of the fiber, and so will provide high light transmission for many wavelengths. For step-index fibers, like those used in this work, light emitted toward one end of the fiber must enter within the acceptance angle for total internal reflection to occur. Via Snell's Law, this angle is related to the critical angle of incidence within the fiber that determines whether or not the light refracts into the medium surrounding the fiber.

In our setup, an optical fiber couples to the xenon flash lamp and an optical fiber feed-through in a 2.75" conflat flange on the cryostat (via ADASMA connectors). The feed-through has a male SMA connection on either end and a short $600\mu\text{m}$ fiber with low attenuation down to 200 nm. The external optical fiber (ThorLabs M114L02) is solarization-resistant and has PVC tubing for protection and ease of handling. The optical fibers inside the cryostat are vacuum-compatible and couple to the other side of the optical fiber feedthrough via vacuum-compatible ADASMA adapters. All of the optical fibers have high UV transmission and a core size of $600\mu\text{m}$. The optical fiber ends are connectorized with SMA connectors. The one exception is the fiber end closest to the photo-cathode which is cleaved. The fibers on the inside of the cryostat pass through a hole in the anode disk to reach the photo-cathode. For testing the first purity monitor design, the optical fiber path on the inside of the cryostat was made up of two fibers coupled together.

There were a few key changes to the optical fiber setup made after finishing testing the first purity monitor design. For one, we replaced the two coupled fibers inside the cryostat with a single fiber to reduce UV transmission losses. We also added an additional optical fiber feedthrough to accommodate simultaneous testing of gold and silver photo-cathodes. This feed-through is also coupled to an optical fiber inside the cryostat. The same external optical fiber is used to make measurements with either photo-cathode by switching which feed-through the fiber is coupled to on the cryostat lid.

3.3 Lenses

In Chapter 5, we describe tests of UV-fused silica lenses (ThorLabs LA4052) as a way to increase the transmission of light to the photo-cathodes. The goal was to increase the purity monitor signal amplitudes by focusing UV light from the flash lamp to increase UV transmission. The lenses are plano-convex and are simulated in Figure 3.3 with light rays emanating from a point source. The focusing ability of the lenses is limited by spherical and chromatic aberrations. These effects can be seen in the simulation in Figure 3.3, where the light rays focus at different points. Spherical aberrations result in varying focal lengths for light rays depending on where they refract on the lens surface. Chromatic aberrations result in a wavelength-dependent focal length. These two effects lead to lower light transmission into an optical fiber. Using two lenses coupled together decreases the focal length and reduces spherical aberration.

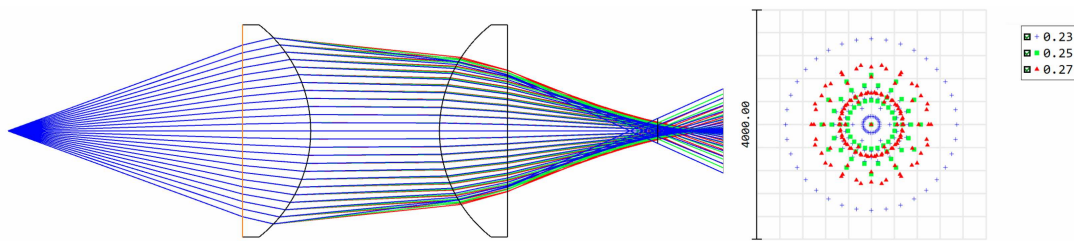


Figure 3.3: Two LA4052 plano-convex lenses simulated in the Zemax program on Sequential mode. The spot diagram on the right is the image of the source at a location optimized with the Spot Size Radial option.

Figure 3.4 shows pictures of the two mounts we have used to hold the optical fiber and lenses. A schematic with distances is shown in Figure 3.5. When the lenses are not being used, the optical fiber is held within a few mm from the glass of the flash lamp bulb to maximize the amount of light that enters the fiber. The fiber mount was made using a threaded aluminum cylinder that holds a Delrin tube containing a trimmed SMA connector to hold the fiber. The base of the lens holder is made of Delrin with eight 8-mm diameter holes that align with the 8-mm diameter ventilation holes at the top of the cooling jacket. A bored Delrin cylinder is placed in two of the ventilation holes to allow the base to mount to the cooling jacket. A 148mm-long cylinder bored to fit 1" lens tubes is affixed to the base. It has small screws equally spaced along the length of the cylinder that



Figure 3.4: The two mounts for the xenon flash lamp and optical fiber. The lens tube holder (left) allows the positioning of the lenses and optical fiber relative to the flash lamp. On the right is the setup that holds the end of the optical fiber close to the glass surface of the bulb.

can be used to fix a lens tube in place. The lenses are placed in a 1.5"-long lens tube with curved sides pointed inward and at a fixed separation of 38.86 mm between their flat sides. They are set in place within the tube by retaining rings. Multiple 1" lens tubes are connected to form a 143mm-long tube. At the end of the tube, the optical fiber is connected to a threaded SMA Fiber Adapter Plate (SM1SMA). This long tube can be moved independently from the lenses and adjusted easily by hand. We found that the easiest way to test a lens setup is to adjust the fiber position by hand to see how the cathode signal changes in real time. The mount is fixed firmly to the end of the cooling jacket by a few threaded metal rods and nuts. Tests of the lenses in vacuum and argon gas are described in Chapter 5.

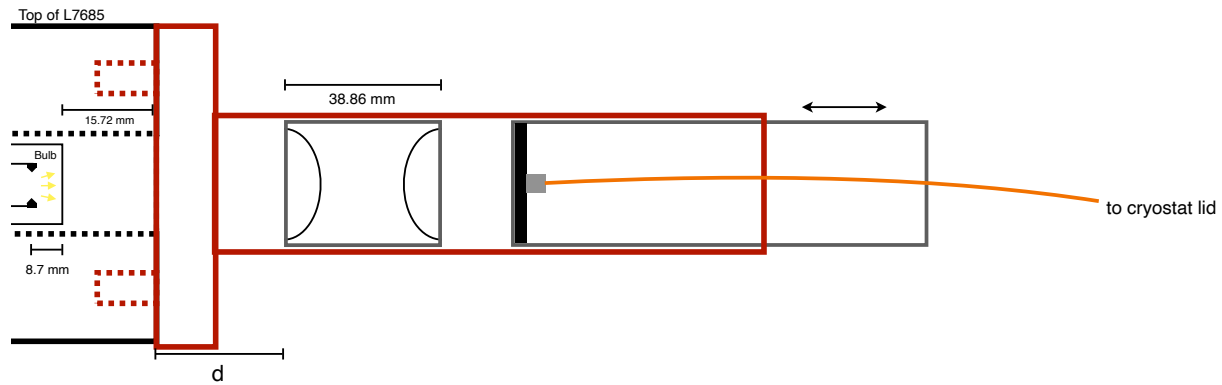


Figure 3.5: Schematic of the lenses mounting apparatus with relevant distances.

Chapter 4

The Purity Monitor

4.1 Overview

To measure LAr purity, a purity monitor must be fully immersed in LAr. When testing each of our purity monitors, they were placed within a cryostat, an insulated and vacuum-tight storage vessel, that is filled with LAr. The first purity monitor was designed at UT Arlington and was tested at CSU with only minor modifications from the original design. We subsequently developed our purity monitor which is 83% longer than the first design. A schematic of our purity monitor design is shown in Figure 4.1.

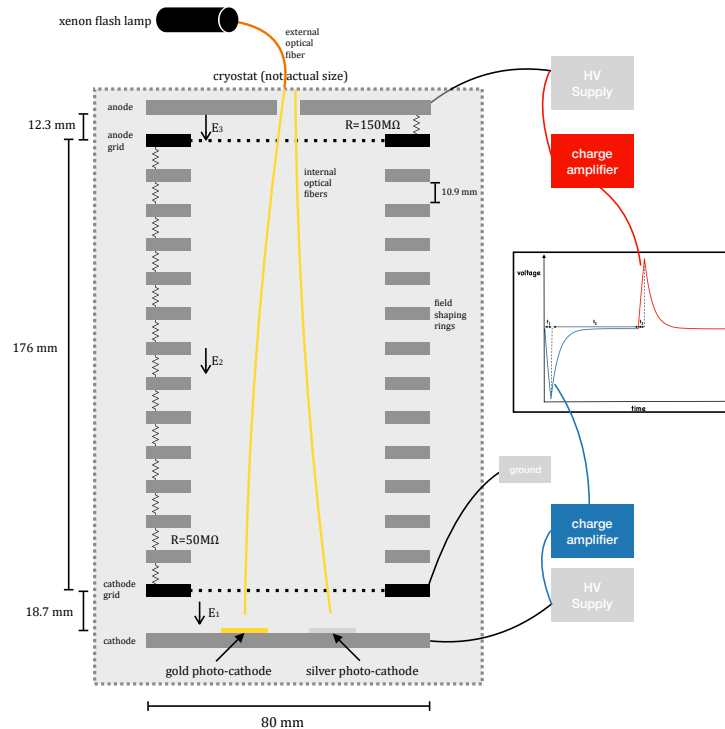


Figure 4.1: Schematic of the CSU-designed purity monitor. Distances are approximate.

The cathode and anode are circular plates made of copper in the first purity monitor and stainless steel in the second purity monitor. On the cathode plate are photo-cathodes, materials sensitive

to the photoelectric effect, for charge production. Once the electrodes are biased with DC voltages, they produce the electric fields that drift electrons to the anode. Wire grids are also used to shield the anode and cathode from induced current caused by the drifting charges. In this chapter, we will discuss the design of the purity monitors in detail.

4.2 Photo-cathodes

The photo-cathode for the first purity monitor comprised four closely packed thin films, each with 100-nm-thick gold coated onto a glass substrate with a titanium adhesion layer. The photo-cathodes were manufactured by Platypus Technologies [18]. Each gold square is held to the surface of the cathode by small metallic clamps, which also provide a conductive connection to the cathode. The second purity monitor has both gold and silver photo-cathodes, which were cleaved from silicon wafers to fit onto the cathode. A 100-nm-thick layer of a photo-electric material was deposited onto each wafer under a vacuum using electron beam evaporation. There is a 5-nm chromium adhesion layer between the photo-cathode and silicon, and the whole wafer itself is 0.525 mm thick. The photo-cathodes were manufactured by Angstrom Engineering [19]. They are held on the cathode via spring lock washers and silver plated screws, which also provide a conductive connection to the cathode. Silver screws are used to avoid cold-welding to the threading in the stainless steel. Figure 4.2 shows the cathodes for both purity monitors.

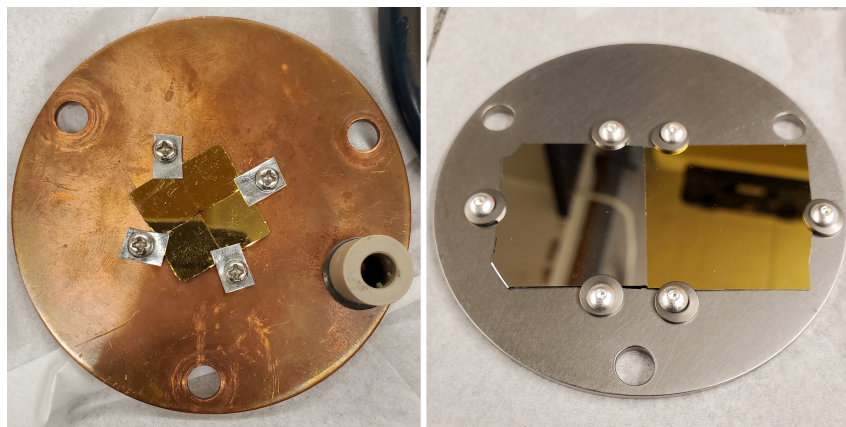


Figure 4.2: The cathodes and photo-cathodes for the first purity monitor (left) and the second purity monitor (right).

If the energy of a photon incident on a photo-cathode surpasses the work function Φ , then an electron can be ejected from the material. The maximum photon wavelength at which this will happen is $\lambda = hc/\Phi$, where h is Planck's constant and c is the speed of light. Gold has a work function of 5.31-5.47 eV [20] depending on the crystal structure, meaning the threshold wavelength for ejecting electrons is 226.7-233.5 nm (UV). Many materials exist that have lower work functions than gold including aluminum with 4.06-4.26 eV, silver with 4.52-4.74 eV, and titanium with 4.33 eV. However, many of these materials readily oxidize when exposed to air. Gold is commonly used for purity monitors because of its inability to oxidize while exposed to air. Even though silver oxidizes over time, we chose to test it as a photo-cathode because it was shown, by NYU Abu Dhabi and UCL, that it produces signals three times larger than gold in a purity monitor in LAr [16].

4.3 Cathode and Anode Grids

There are three different electric fields in the purity monitors due to the presence of two wire grids, one near the cathode and one near the anode. Without proper shielding, induced currents, caused by the drifting charges, could be produced on the cathode and anode during the entire electron drift time [21]. This would extend the time over which the charge amplifiers would need to integrate the current.

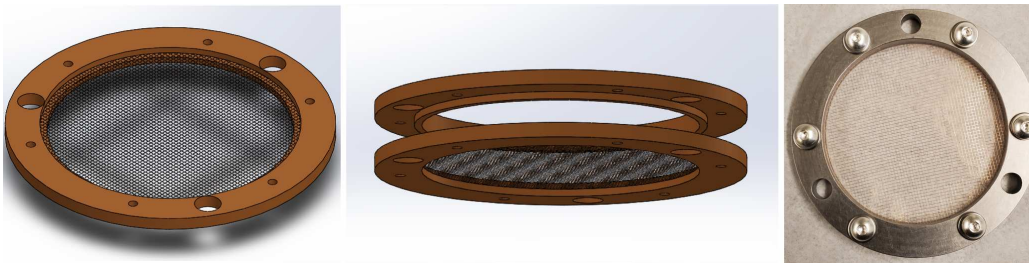


Figure 4.3: The grids for the CSU purity monitor. The first two images are from a Solidworks model and show how a mesh is placed between two rings. The third image is one of the completed grids.

The grid design for the first purity monitor is based on that of the Liquid Argon Purity Demonstrator [15]. Each grid is made of two G10 rings held together, each with a surface of copper. Parallel wires are soldered to the surface of each ring. The two rings are oriented 90 degrees relative to the other. We designed our purity monitor grids based on that of NYU Abu Dhabi and UCL [16]. The grid wires are in the form of electro-formed copper meshes (MC7) manufactured by Precision Eforming. We cut out circular meshes from an 11" by 11" sheet and pinched them between two stainless steel rings. The rings are held together by silver-plated screws and conical spring lock washers. The wire radii and spacing for the two grid designs are listed in Table 4.1.

Bunemann et al. [21] investigated the prospects of using wire grids to shield electrodes from induced current. They derived multiple equations that describe the shielding ability of wire grids. The equations were verified experimentally and assume that the wire radius, r , and wire separation, d , are the same for all wires in a grid. The two most relevant equations for purity monitors describe the grid-shielding inefficiency, σ , and the condition for maximum drift electron transparency. The shielding inefficiency is

$$\sigma = \frac{l}{p+l} \quad (4.1)$$

p is the distance from the grid to the electrode being shielded. An inefficiency of 0% means that no charges behind the grid induce currents on the electrode being shielded. In equation 4.1,

$$l = \frac{d}{2\pi} \left(\frac{1}{4}\rho^2 - \ln \rho \right) \quad (4.2)$$

and

$$\rho \approx 2 \times \frac{2\pi r}{d} \quad (4.3)$$

The extra factor of 2 in equation 4.3 is added because the grids have two layers of parallel wires. To minimize σ , l must be sufficiently small relative to p . Electrons must also not get absorbed by the grids as they drift to the anode as this reduces how much charge arrives at the

anode. If electrons are absorbed by the grids, the apparent electron lifetime will be lower than the true electron lifetime, hence leading to systematic error in the measurement. To have no electrons absorbed by a grid (100% transparency), the following two conditions must be satisfied:

$$\frac{E_2}{E_1} > \frac{1 + \rho}{1 - \rho} \quad (4.4)$$

and

$$\frac{E_3}{E_2} > \frac{1 + \rho}{1 - \rho} \quad (4.5)$$

The cathode field, E_1 , is the field between the cathode and cathode grid, the drift field, E_2 , is the field between the cathode grid and anode grid, and the anode field, E_3 , is the field between the anode grid and anode. There are three fields because purity monitors have two grids. In both equation 4.4 and equation 4.5, ρ takes on the same value since the cathode and anode grids have the same wire radius and spacing. By rearranging equations 4.4 and 4.5, we find that

$$\frac{1 + \rho}{1 - \rho} E_1 < E_2 < \frac{1 - \rho}{1 + \rho} E_3 \quad (4.6)$$

The wire radii, spacing, and calculated inefficiencies for the grids used in both purity monitors are shown in Table 4.1. The required field ratios to have maximum grid transparency are also listed.

Table 4.1: Grid parameters, inefficiencies, and field ratios for the purity monitor grids. The field ratios are the calculated minimum required field ratios for the cathode and anode grids to maintain grid transparency.

Purity Monitor Version	radius r [mm]	wire spacing d [mm]	σ_c [%]	σ_a [%]	Field Ratio
First	0.05	3	3.99	4.10	1.53
Second	0.0315	0.953	0.742	1.12	2.42

4.4 Electric Fields

The cathode grid is connected to ground, and the cathode and anode are biased to a negative and positive voltage, respectively. Two SRS high voltage power supplies bias the anode and cathode. The bias voltages force the fields to point toward the cathode which causes the photo-electrons to drift toward the anode. A series of stainless-steel field-shaping rings between the anode grid and the cathode grid forms a voltage divider. This produces a corresponding voltage drop across each resistor that connects adjacent rings. The voltage at the anode, V_A , is slightly lower than the voltage set on the power supply by about 2-3% due to a voltage drop across the HV filter. A resistance is connected between the anode and anode grid to fix E_3/E_2 . All resistances and relevant distances are listed in Table 4.2.

Table 4.2: Characteristics and measurements of the purity monitors for the tests described in this work.

Characteristic	Original Design	New Design
Cathode, anode disk thickness	2 mm	2.6 mm
Cathode, anode, ring diameter	82 mm	80 mm
Cathode Grid-Cathode Gap	13.5 mm	18.7 mm
Gap between rings	13.7 mm	10.9 mm
Ring Thickness	2.3 mm	2.0 mm
Anode Grid-Anode Gap	14.6 mm	12.3 mm
Grid Ring Thickness	4.00 mm	4.94 mm
Total Cathode-Anode Drift Distance	96.37 mm	176.4 mm
Number of Field-Shaping Rings	4	12
Resistance between anode and anode grid	150M Ω	125M Ω
Total resistance	400M Ω	775M Ω

E_2 is determined by the distance between the two grids and their potential difference. This means the second purity monitor needs a higher anode voltage than the first purity monitor to maintain the same drift field due to its larger grid-grid separation. Figure 4.4 shows a FreeFEM [22] simulation of the fields in the second purity monitor. The equal spacing of the equipotential lines means the field is uniform.

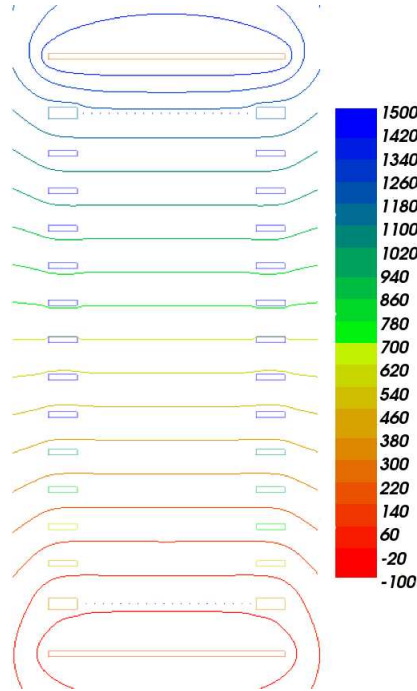


Figure 4.4: A 2D cross-section equipotential field map of the CSU purity monitor made using the FreeFEM finite element software. The color scale is in volts and the distances are approximate. The cathode is at the bottom.

The first purity monitor had $150\text{M}\Omega$ between the anode and anode grid, which sets $E_3/E_2 = 2.82$. This satisfies the field requirement in Table 4.1 for maximum grid transparency. The second purity monitor had $125\text{M}\Omega$ between the anode and anode grid, which sets $E_3/E_2 = 2.22$. This is lower than the field requirement in Table 4.1, so we later changed this to $150\text{M}\Omega$ which makes $E_3/E_2 = 2.66$. In the tests described in this work, however, the second purity monitor has $125\text{M}\Omega$. The cathode bias voltage can be adjusted to ensure that the ratio E_2/E_1 satisfies the field ratio requirement.

4.5 Installation and Tests

We mounted the purity monitors to a G10 structure that is fixed to a star-shaped flange (see Figure 4.5). The star-shaped flange has three 2.75" conflat flanges that house the optical fiber feedthroughs and high-voltage feedthroughs. We use a hanger to raise and lower a purity monitor into and out of the cryostat. The hanger makes inserting, removing, and inspecting the purity

monitor straightforward. The purity monitor is resistance-tested with an AEMC megaohmmeter before insertion to verify the total resistance from the anode to the cathode grid.



Figure 4.5: Purity monitor resistance test before cryostat insertion (left), full purity monitor apparatus and hanger (center), and top of purity monitor flange (right).

The majority of the second purity monitor was cleaned with an ultrasonic cleaner. The stainless steel components were also cleaned with degreaser before they were first used. The photo-cathodes and wire grids were more gently cleaned by blowing on them with low-pressure nitrogen gas. We also clean the interior of the cryostat with Kimwipes and 2-propanol before inserting the purity monitor. Once the entire apparatus is cleaned and the purity monitor is ready for tests, it is inserted into the cryostat which is then sealed. Figure 4.6 shows the lid of the cryostat for tests of both purity monitors.

After the first purity monitor was decommissioned, we added a second optical fiber feedthrough and swapped the SHV-10kV high-voltage feedthrough with an SHV one for tests of the second purity monitor. After the first LAr test of the second purity monitor, we moved the anode high-voltage connection to a separate feedthrough to eliminate discharging caused by raising the anode voltage too high. This change is not reflected in Figure 4.6.

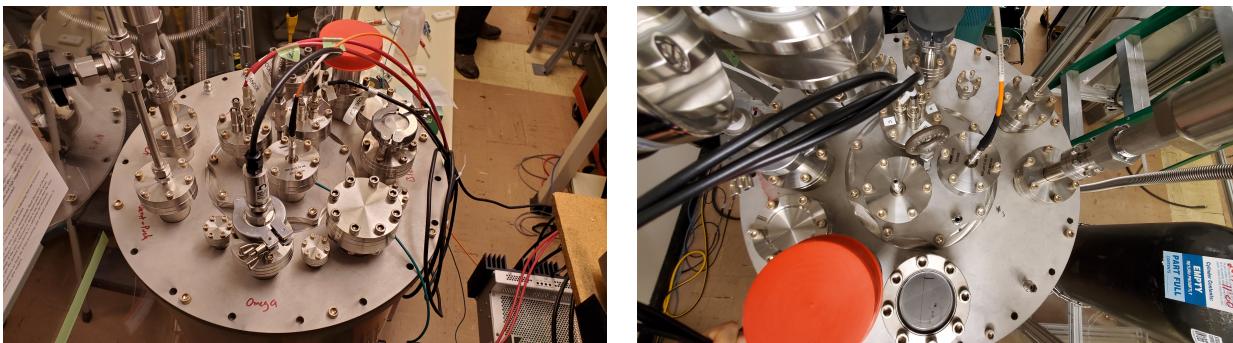


Figure 4.6: The cryostat lid when testing the first purity monitor (left) and when testing the second purity monitor (right).

We tested the purity monitor resistors in liquid nitrogen to determine if the resistance changes at cryogenic temperatures. The setup for this test is shown in Figure 4.7. We slowly inserted the resistors into a small insulated container. We tested two resistor combinations, one with a $50\text{M}\Omega$ resistor and a second with $175\text{M}\Omega$ made using $25\text{M}\Omega$, $50\text{M}\Omega$, and $100\text{M}\Omega$ in series. Each resistor chain was soldered to high-voltage wire on both sides. A megaohmmeter was connected to the end of each wire to measure the resistance. We used the 1000V setting on the meter to get the most accurate resistance reading. Shortly after the resistors were submerged, the resistances increased by about 5%. After 7 hours of being submerged, the resistances stayed stable at about 5% higher than the initial resistance when in the air. The resistances returned to room-temperature levels once removed from liquid nitrogen and allowed to warm up.



Figure 4.7: Resistance and robustness test of the purity monitor resistors.

Chapter 5

Purity Monitor Tests

5.1 Vacuum Performance

We use an Edwards ESDP12 scroll pump and an Edwards nEXT85D turbo pump to evacuate the cryostat. To begin cryostat evacuation, we turn on the scroll pump to bring the internal cryostat pressure to less than about 5 mbar. Once the pressure is low enough, we turn the turbo pump on to lower the pressure to as low as about 10^{-4} mbar. The cryostat evacuation helps to remove impurities and trapped gases from the purity monitor apparatus and cryostat. To improve this process, we fill the cryostat with high-purity argon gas to near 1 atm after the cryostat has been sufficiently evacuated. Then, we evacuate the cryostat again until the pressure does not change appreciably over a few minutes. We repeat this procedure a few more times before filling the cryostat with LAr. Figure 5.1 shows the setup when doing vacuum tests.

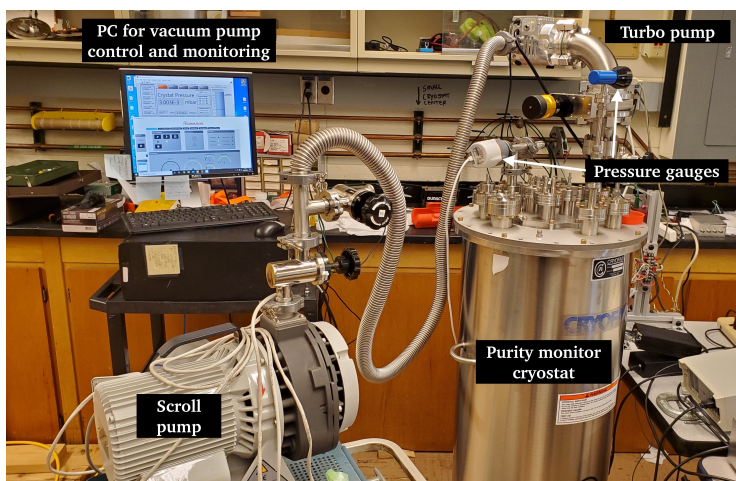


Figure 5.1: The setup used to test the purity monitors in a vacuum. This setup was moved and modified for tests in LAr.

The signals in a vacuum are very large compared to signals in gaseous argon and LAr. We utilize this large signal-to-noise ratio to measure the gain ratio of the charge amplifiers with low

uncertainties from signal fluctuations. Since our cryostats are always evacuated before filling them with LAr, testing the purity monitor in a vacuum is a convenient way to check that all the connections are correct and signals can be seen from the cathode and anode. However, depending on the cryostat pressure, the signals can be slightly or heavily distorted in a vacuum. For instance, at a pressure around 10^{-1} to 10^{-2} mbar, the distortions are prominent. Figure 5.2 shows an example of this effect. It shows the charge amplifier voltage output and the reconstructed current I_{reco} at a pressure of 5×10^{-1} mbar.

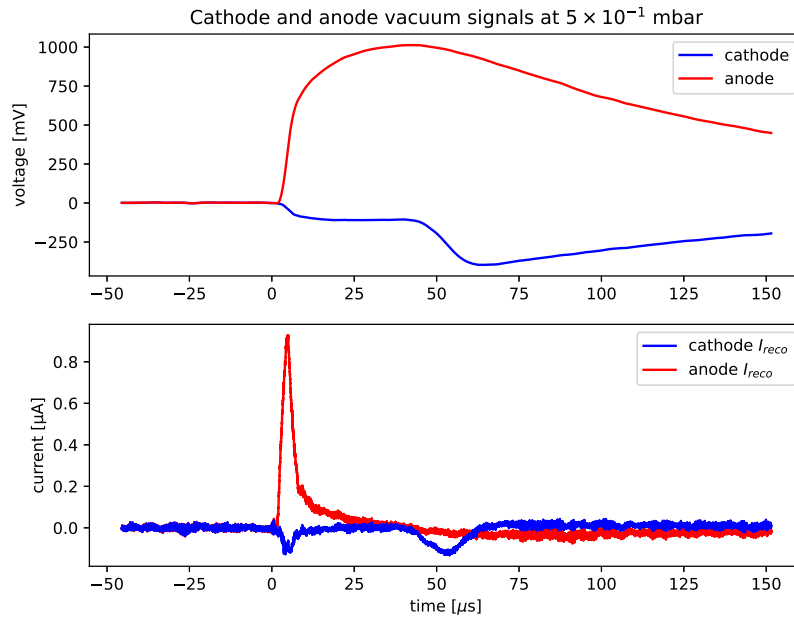


Figure 5.2: Cathode and anode signals in a vacuum using the first purity monitor at 5×10^{-1} mbar. $V_C = -90V$ and $V_A = 500V$. The charge amplifier capacitance is assumed to be 5 pF when calculating the reconstructed current. The signals undergo a rolling average to smooth out the reconstructed current plot.

The cathode signal is distorted and much smaller than the anode signal. The reconstructed current shows peaks for both signals at about $5\mu s$ that most likely correspond to the photo-electron current. The cathode signal has a secondary current spike near $50\mu s$. We have not observed similar behavior in gaseous argon or LAr. One explanation for this observation is that the photo-electrons ionize gas molecules, resulting in positive ions slowly drifting to the cathode which explains the

secondary current spike in the cathode signal. The resulting ionization electrons would rapidly drift to the anode, which explains how the anode signal is so much larger than the cathode signal. It should be noted that for the data shown in Figure 5.2, $E_2/E_1 = 0.7$ which is not sufficient for maximum grid transparency. This would reduce the anode signal amplitude and not make it larger, so it cannot explain how the anode signal is larger than the cathode signal. Figure 5.3 shows another example of a cathode signal and reconstructed current in vacuum, now in the second purity monitor.

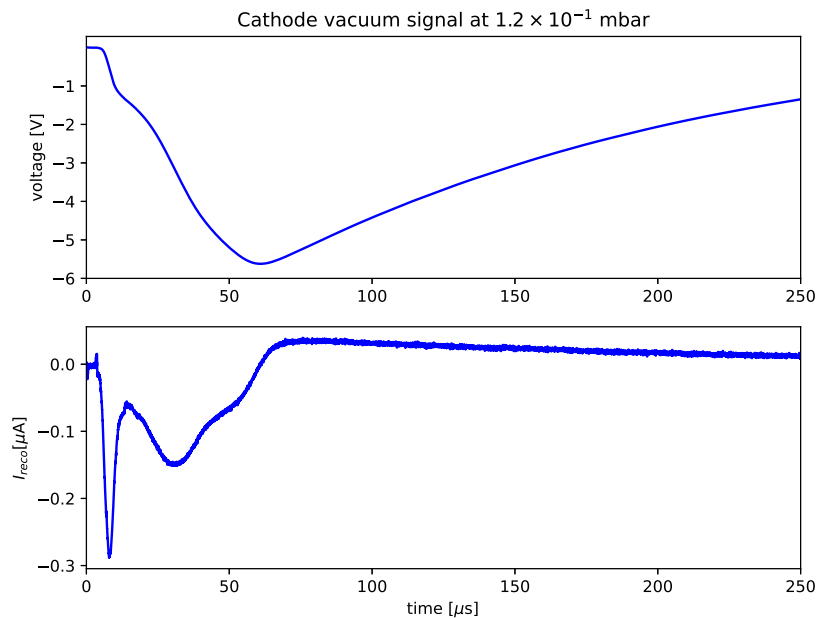


Figure 5.3: Cathode signal in a vacuum using the second purity monitor at 1.2×10^{-1} mbar. $V_C = -25\text{V}$ and $V_A = 450\text{V}$. The charge amplifier capacitance is assumed to be 1 pF when calculating the reconstructed current. The signals undergo a rolling average to smooth out the reconstructed current plot.

To eliminate this effect in the signals, the pressure needs to be sufficiently low in the cryostat. For example, we show in Figure 5.4 with the second purity monitor that the effect disappears at 1.8×10^{-4} mbar. The cathode and anode signals also have a very similar shape and size, which we expect since there are very few impurities to attenuate the photo-electrons at this pressure. The differing charge amplifier gains, charge amplifier RC effect, and the presence of cross-talk

influence the shapes and amplitudes of the two signals. It should be noted that in the data shown in Figure 5.4, $E_3/E_2 = 2.22$ (fixed) and $E_2/E_1 = 2.0$ at these voltages which are not sufficient for maximum grid transparency. This means the anode signal may have been reduced due to grid transparency. Figures 5.2 and 5.4 show that sufficiently low pressures are required to have the best purity monitor performance in a vacuum. We also observed that the anode voltage could not be raised to more than 400V-500V without seeing substantial noise in the signals. We think this was due to discharging in or near the HV feedthrough.

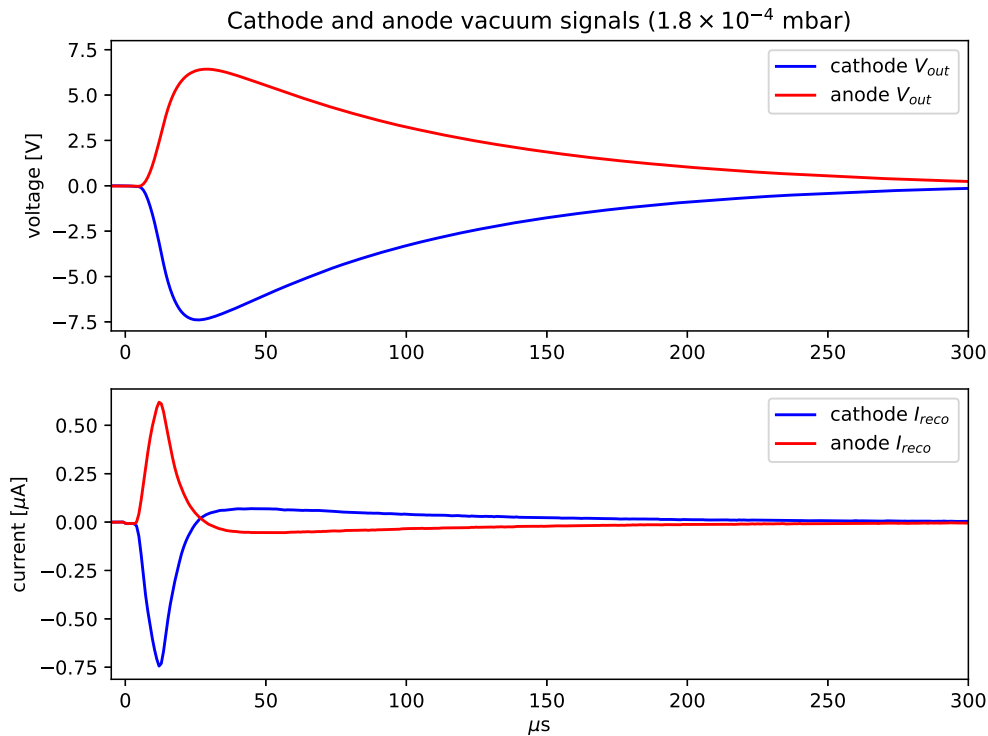


Figure 5.4: The cathode and anode signals observed in vacuum using the second purity monitor at 1.8×10^{-4} mbar with $V_C = -16\text{V}$ and $V_A = 300\text{V}$. The capacitances of the charge amplifiers are assumed to be 1 pF for calculating the reconstructed current.

5.2 Initial Purity Monitor Tests in LAr

5.2.1 Experimental Setup and Tests

Now we will discuss LAr tests with the first purity monitor design. This design used gold as a photo-cathode and was 9.6 cm long. It was also used along with the Excelitas PAX-10 xenon flash lamp. Figure 5.5 shows the LAr experimental setup for all purity monitor LAr tests. The cryostat containing the SingleCube detector is on the left, while the cryostat (Cryofab model CF-1436-F) containing the purity monitor is on the right. The two are connected via an isolated transfer pipe that allows the flow of gas or LAr when valves are opened. The LAr used in the purity monitor tests is filtered. The filters are located inside the large cryostat. One is an oxygen getter (GetterMax 133) that removes oxygen and the second is a molecular sieve (RCI-DRI-13X) that removes water.



Figure 5.5: Experimental setup for purity monitor LAr tests.

We tested the purity monitor once it was entirely covered by LAr. The liquid slowly boiled away and was not cooled. By filling the small cryostat nearly full of LAr, we had multiple days to take data before the liquid-level fell below the top of the purity monitor. We began by turning on the flash lamp and the voltages for the cathode and anode. We looked for signals on the oscilloscope. The oscilloscope acquisition was triggered by a pulse from the pulse generator that

triggered the flash lamp. We tried to uncover signals by averaging traces and performing background subtractions. The highest voltages we used were $V_C = -100V$ and $V_A = 1300V$. In the first LAr test, we did not observe any cathode or anode signals. There were problems with the electronics system during this first run, which might have prevented signals from appearing. In the second LAr run, we were still unable to see cathode or anode signals. This time, there were no signs of electronics issues that could explain the absence of signals. We know this because we could see cathode and anode signals in vacuum right before the LAr fill. The cathode signal being absent means that it must have been too small to measure. And due to the charge attenuation by impurities, the anode signal would also likely be too small to measure.

5.2.2 Factors Impacting Signal Size

Now we will discuss the factors that can affect signal size in a purity monitor. First of all, presence of impurities can have a large impact on the anode signal size. This is because impurities can reduce Q_A to such an extent that the S/N would be too low to see a signal from the anode. But since we do not see cathode signals at this stage, it is most crucial that we understand what impacts the cathode signal size. The size of a signal depends strongly on the total charge extracted from the photo-cathode, but the actual observed signal is shaped by the charge amplifier RC effect and the electron lifetime. However, the total charge extracted can be changed by modifying the setup, while there is not too much we can do to reduce the other two effects. Therefore, the best way that we have to increase the size of signals is to increase the production of photo-electrons. Photo-electron production depends primarily on

1. the intensity of UV light hitting the photo-cathode
2. the photo-cathode work function
3. the cathode field strength, E_1

Increasing the intensity of UV light hitting the photo-cathode will increase the amount of electrons that can be ejected from the material. This can be accomplished by using a light source

that makes more UV light and by increasing the UV light transmission to the photo-cathode. To increase UV light intensity, we use the Hamamatsu lamp that has about 10 times more energy per flash than the Excelitas lamp. We also worked to improve the UV transmission by modifying the optical fiber setup. The optical fibers inside the cryostat have been two coupled together for ease of assembly. We determined that there is substantial light loss when connecting two fibers together like this, so we replaced these with a single uninterrupted optical fiber. Using lenses may also improve transmission by focusing light into the optical fiber.

Decreasing the work function of the photo-cathode can also increase the amount of photo-electrons ejected from the material. This is because the higher wavelength photons in the xenon flash lamp spectrum can be utilized to produce photo-electrons. While gold is a common photo-cathode in purity monitors, there are numerous materials with lower work functions. One of the issues with these materials is that they oxidize which may reduce their performance in a purity monitor. Manenti et al. [16] tested various photo-cathodes in a purity monitor. They found that silver had the best performance, producing signals about three times larger than gold in LAr. In the next section we discuss tests we performed of silver and gold photo-cathodes. The goal is to verify that silver can produce larger signals than gold.

Increasing the cathode field strength is expected to increase the cathode signal size. Ref. [16] demonstrates that this is the case in LAr with gold and silver photo-cathodes. One benefit of this method is that it does not necessarily require modifications to the purity monitor itself, since it simply requires raising the cathode voltage. If the cathode signal is being studied on its own, raising the cathode voltage is all that is required. However, when trying to measure electron lifetime, then E_2 and the anode voltage must be raised as well to maintain grid transparency. We have encountered limitations to the technique of raising E_1 for this reason. In particular, we have observed discharges inside the cryostat due to high anode voltages. We have also determined that voltages above 1kV are beyond the voltage rating of our HV filters. These issues are discussed more later, but they pose as limitations for raising E_1 if not properly handled. The field dependence of cathode signals in LAr is explored experimentally later.

5.3 Increasing Signal Size

5.3.1 Gold vs. Silver Signals

We performed a variety of tests of the second purity monitor in gaseous argon. One of the things we investigated is the difference between using gold and silver photo-cathodes. Figure 5.6 shows an example of anode and cathode signals in high-purity gaseous argon with both photo-cathode types. Firstly, we see that the signals in gaseous argon are much smaller than signals in vacuum, in particular over 100 times smaller. The S/N is reduced compared to a vacuum, which causes the xenon flash lamp noise, that is seen around $0 \mu\text{s}$, to be clearly visible in the traces. We also see in Figure 5.6 that the signals obtained with silver are larger than those obtained with gold.

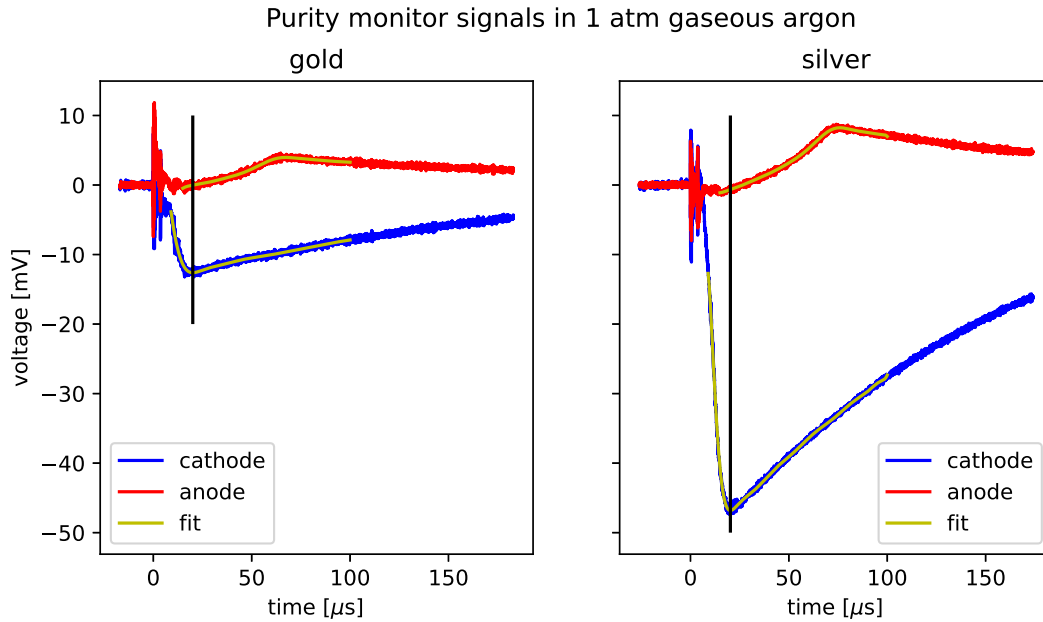


Figure 5.6: Cathode and anode signals in the second purity monitor for gold and silver. Yellow lines denote polynomial fits and black vertical lines denote the locations of the cathode peaks. $V_C = -50V$ and $V_A = 1000V$.

In this case, the silver-over-gold ratio is 3.71 for the cathode signals and 2.07 for the anode signals. There is some difference in the light transmission in the two fibers which we have not quantified at this point. A followup study is needed to better quantify and explain the differences between the light transmissions of the two optical fibers. The anode signals also appear to begin

around the time that the cathode signals reach a peak. We have placed black vertical lines at the cathode peak to make it easier to see when the anode signal begins. We expect that t_1 should be greater than t_3 . This is because $E_3 > E_1$ and the distance between the anode and anode grid is shorter than the distance between the cathode and cathode grid. However, clearly the opposite is true in Figure 5.6. This behavior may be caused by induced current from the drifting electrons. It may be due to a combination of the $>0\%$ inefficiency of the grids and the fast drift speed in gaseous argon. The behavior was still present after inspecting and replacing the grids. Given the similarity of our grids and setup to that of Ref. [16], who have the same grid manufacturer and similar grid parameters, we do not expect that our setup will produce similar behavior in LAr.

Figure 5.7 shows another example of cathode signals obtained with gold and silver. In this case, at $V_C = -50V$, the silver-over-gold ratio is 4.51. At $V_C = -100V$ and $V_C = -150V$, we measured ratios of 3.83 and 3.89, respectively. It is clear from these measurements that silver can produce cathode signals over three times larger than gold with our setup. This can be at least partly explained by the fact that silver can utilize more of the xenon flash lamp spectrum than gold. These results mean that silver can produce more photo-electrons than gold in our setup, likely due to its lower work function.

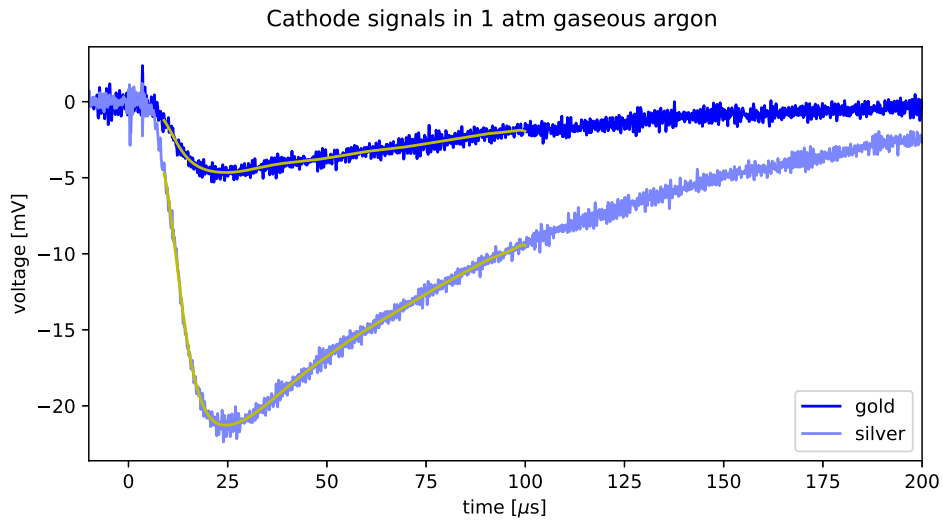


Figure 5.7: Example of cathode signals in the second purity monitor for gold and silver. Yellow lines denote polynomial fits. $V_C = -50V$ and the anode power supply is turned off.

A potential followup study would be to compare the signals obtained with gold and silver in LAr, while also quantifying the optical fiber differences. We have used the same silver photo-cathode piece for all tests of the second purity monitor up to this point. It would be interesting to compare this silver photo-cathode to gold as a part of this followup study. This is because silver will oxidize over time, while gold will not. It is important to understand how the silver photo-cathode changes over time while being exposed to air. To be clear, the photo-cathodes are exposed to air a vast majority of the time.

5.3.2 Xenon Flash Lamp Signals Comparison

Here we show the results of a study comparing the signal amplitudes in the second purity monitor as a function of photo-cathode and xenon flash lamp. Figure 5.8 shows the signals obtained with each photo-cathode and each xenon flash lamp.

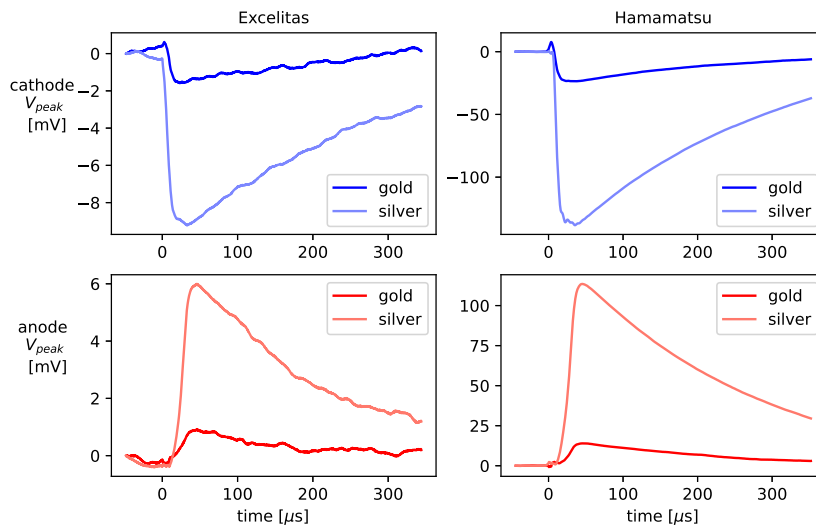


Figure 5.8: Purity monitor signals as a function of xenon flash lamp and photo-cathode. The optical fiber was positioned a few millimeters away from the surface of the bulb for each lamp. We used a noise trigger for both flash lamps. $V_C = -50\text{V}$ and $V_A = 1100\text{V}$.

We find about 15 times larger signals with the Hamamatsu lamp than with the Excelitas lamp for both gold and silver. For comparison, we have seen silver increase the signal size by a factor of

3-4 prior to this test. It is clear that upgrading the flash lamp had a much larger impact on the signal size than changing the photo-cathode. It is not surprising that this result is the same with gold and silver since both xenon flash lamps have nearly identical spectra. The dramatic performance boost with Hamamatsu is also not a surprise since the lamp has about ten times more energy per flash compared to the Excelitas lamp. The improvement in signal size with the Hamamatsu lamp and the silver photo-cathode means we were successful in upgrading the system in such a way to make larger signals.

The cathode and anode signals for the combination of the Excelitas lamp and gold photo-cathode give us insight into how large the signals would have been in the LAr tests of the first purity monitor. Those signals are each less than 2 mV. If the signals in LAr are smaller than they would be in gaseous argon, this would mean the signals would be even smaller than 2 mV and more difficult to see. Since in LAr the drift speed is much lower than in gas, the attenuation of the photo-electrons due to impurities would likely be larger. As a result, the LAr anode signals would be even smaller than the signals observed in gas. This leads us to the conclusion that the first purity monitor setup was likely not sufficient for seeing signals in LAr.

It should be noted how in Figure 5.8 the silver-over-gold ratio is closer to 5-6, compared to 3-4 as shown earlier. We have not determined what caused this change, but potential causes are light transmission differences in the two optical fibers or physical changes in either of the photo-cathodes. The former is possible given that the optical fiber setup has been modified a few times. For instance, their positions and orientations have been adjusted which may have had an impact on light transmission. The latter possibility can only be explored once light transmission has been either ruled out or quantified as a cause of signal size differences.

5.3.3 Lenses Performance

We tested lenses as another way to increase signal size. The lenses tests were performed in gaseous argon and vacuum. In particular, we measured the cathode amplitude in various lens configurations in a vacuum with a pressure of 1.7×10^{-4} mbar and in gaseous argon with a pressure of about 1 atm. To set up the vacuum, we would run the pumps until we reached a stable pressure. This is also a pressure at which there are stable and non-distorted signals. The tests described here were performed while the pumps were running to keep the pressure stable throughout data-taking. We made measurements of cathode signal size in two general configurations, both of which are described and shown in Chapter 3. One configuration uses no lenses and places the optical fiber close to the flash lamp bulb. The second configuration uses lenses that are placed in the lens mount. A schematic is shown in Figure 3.5 in Chapter 3. The lenses were fixed in place for each signal measurement while the optical fiber was moved by hand. For each measurement, we placed the lenses at a different distance from the end of the flash lamp. As the flash lamp was running, we moved the optical fiber by hand until we saw the signal amplitude on the oscilloscope reach a maximum. We saved traces in the oscilloscope for gold and silver only when the maximum signal size was found. After making a measurement, the position of the lenses, d , was adjusted slightly. Then, the fiber position was adjusted once again by hand until the maximum signal size was found. This process was repeated for various values of d , which were measured with calipers. Figure 5.9 shows the result of this test in a vacuum.

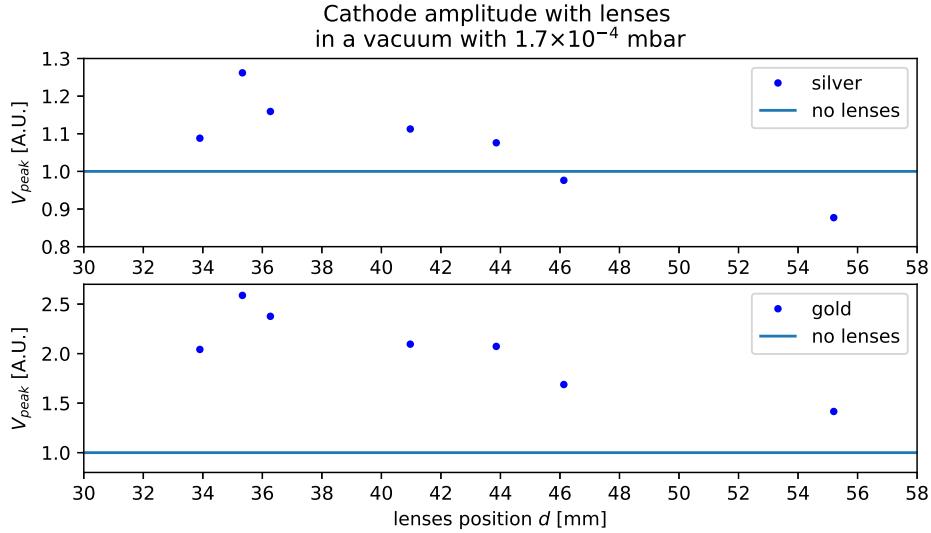


Figure 5.9: Cathode amplitude for both photo-cathodes as a function of lens position d in a vacuum. The amplitudes are normalized to the amplitude measured without lenses, which is indicated by a horizontal line at 1. The blue line represents 557.4 mV for gold and 8328 mV for silver.

We determined that, in the range we tested, the maximum signal amplitudes are found at about $d = 35$ mm for gold and silver in a vacuum. The signal amplitudes are very sensitive to lens position near the maximum; just 1 mm up or down made a big difference in the signal size. The largest signals are found between 32 and 36 mm for both gold and silver. We observed the largest signals at about 35 mm for gold and silver. The signals are larger than the no-lenses setup by a factor of 2.57 for gold and 1.26 for silver. The improvement with silver is modest, while the improvement with gold is fairly promising. These results show that lenses do improve the signal size in a vacuum, but the results may be different in gaseous argon and LAr. Next we will assess the performance of the lenses in gaseous argon.

The results of a test in gaseous argon is shown in Figure 5.10. Similarly to the results in a vacuum, gold has a larger improvement with lenses compared to silver. At a distance of less than 36 mm, gold has an improvement of 1.5-2.0, and silver has an improvement of about 1.2-1.3. The maximum values are 2.01 and 1.34 for gold and silver, respectively, at 35.7 mm. Gold also sees an improvement of about 1.4-1.5 at distances of more than 38 mm, while silver's improvement over that range is about 1.1. Gold appears to have a smaller maximum improvement compared

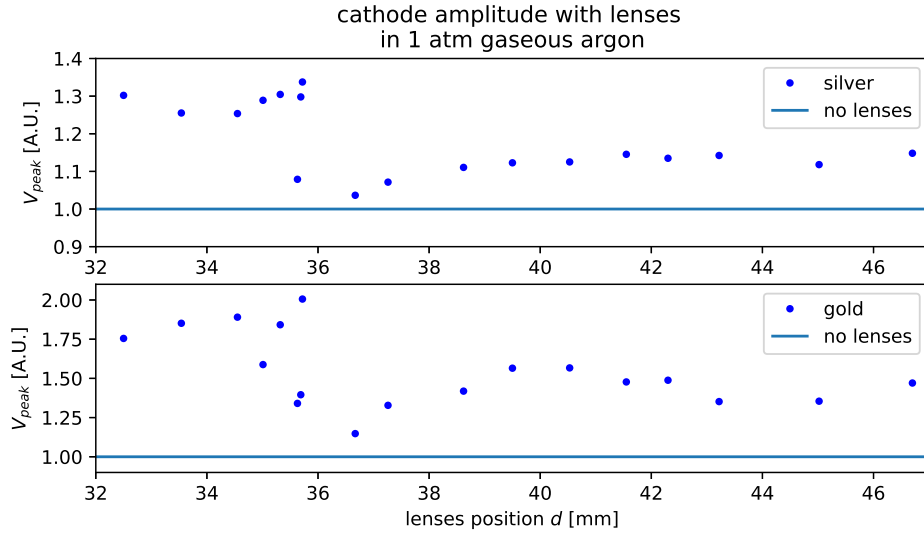


Figure 5.10: Cathode amplitudes for both photo-cathodes as a function of lens position d ($V_C = -50V$). The amplitudes are normalized to the amplitude measured without lenses, which is indicated by a horizontal line at 1. The blue line represents 47.8 mV for gold and 528.9 mV for silver.

to vacuum, while silver has close to the same improvement compared to vacuum. Further testing needs to be done in LAr to determine if similar results are obtained in that medium. The lenses can be tested in additional ways, such as by using distances smaller than 32 mm, varying the lens separation, and testing the cathode field dependence.

5.4 Density Dependence of Signals in Gaseous Argon

We have studied the cathode signal size and drift time as a function of cryostat pressure. Since the volume and temperature in the cryostat are constant, the argon density increases as gas flows into the system and as the pressure increases. We evacuate the cryostat and then allow high-purity gaseous argon to slowly flow in. We stopped the flow whenever the internal pressure increased by about one psi and took a measurement of the cathode signal. We repeated this process until the pressure reached atmospheric pressure. The results for the cathode signal amplitude and the peak-to-peak time, t_2 , are shown in Figure 5.11.

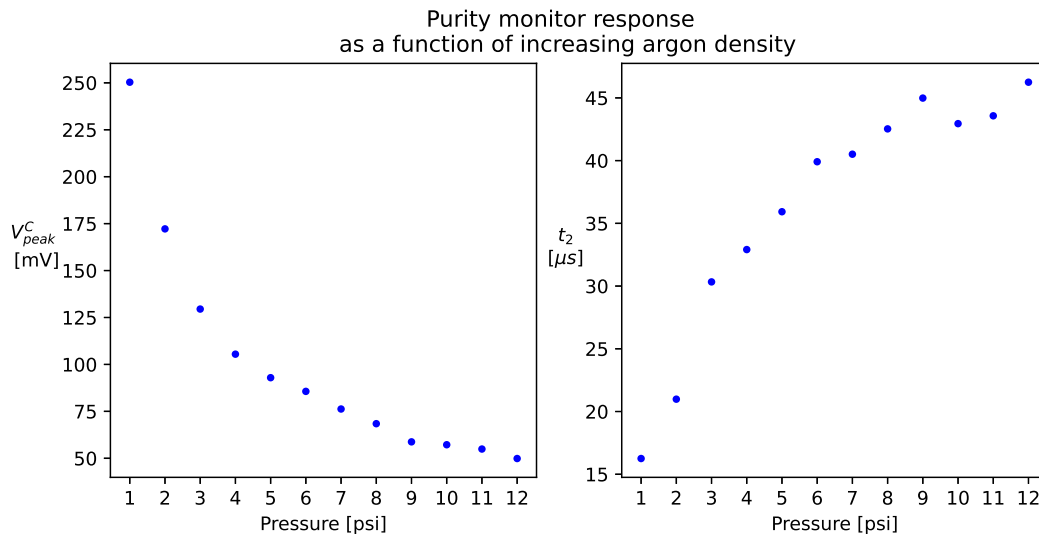


Figure 5.11: Cathode V_{peak}^C and t_2 are shown as a function of cryostat pressure. The silver photo-cathode is used in the second purity monitor for this test. $P = 12$ psi is approximately atmospheric pressure in Fort Collins, Colorado where this test took place. Each value is extracted from the average of 100 single traces with a polynomial fit.

We see in Figure 5.11 that the cathode amplitude decreases and the drift time increases when argon density increases. These results mean that, if extrapolated to higher densities, the signal amplitudes will be smaller and the drift velocity will be slower at the density of LAr. This means that for all the purity monitor signals that we observe in gaseous argon, the corresponding signals in LAr will be more far apart in time and smaller in amplitude. To compensate for the decreased

cathode amplitude in LAr, we can increase the cathode field magnitude as a way to increase S/N.
This study does not take into account the temperature change between gaseous argon and LAr.

5.5 LAr Tests with Upgraded Purity Monitor

5.5.1 Changes to the Purity Monitor Setup

In this section we discuss tests of our new purity monitor design in LAr. The purity monitor length has been increased from 9.6 cm to 17.6 cm, and silver is used as the primary photo-cathode. The electronics and hardware were set up the same as shown in Figure 2.7, the power and ground isolation system was used, and the tests were performed in the same location as previous LAr and gaseous argon purity monitor tests. The primary differences between testing the old and new purity monitor designs in LAr are shown in Table 5.1.

Table 5.1: Primary differences between testing each purity monitor design in LAr.

	Original Design	New Design
Total Length [mm]	96.37	176.4
Photo-cathode	Gold	Silver
Light Source	Excelitas PAX-10	Hamamatsu L7685

The most crucial differences are the total purity monitor length, the photo-cathode used, and the light source used. The last two of these changes will lead to an increase in both the cathode and anode signal sizes, which is a result informed by the tests in an earlier section. The first of these changes only affects the anode signal size. This is because a longer total drift length leads to a longer total drift time, meaning that more electrons will be attenuated before reaching the anode. With a lower Q_A , the anode peak voltage Q_A/C will be smaller as a result. This means that with a sufficiently low electron lifetime, we could see a cathode signal but not an anode signal.

Two separate tests of the new purity monitor design were performed in LAr, each with a different batch of LAr. The LAr was filtered once before filling the cryostat. In both of these tests, we observed cathode signals and no anode signals.

5.5.2 Cathode Signals and Field Dependence

Figure 5.12 shows averaged cathode signals observed in LAr during the second test at various cathode voltages. To see clearer signals, a background subtraction is used to reduce the xenon-flash-lamp induced noise near $t = 0$. A background signal is created by averaging traces while the xenon flash lamp is running and the optical fiber is disconnected from the cryostat feed-through.

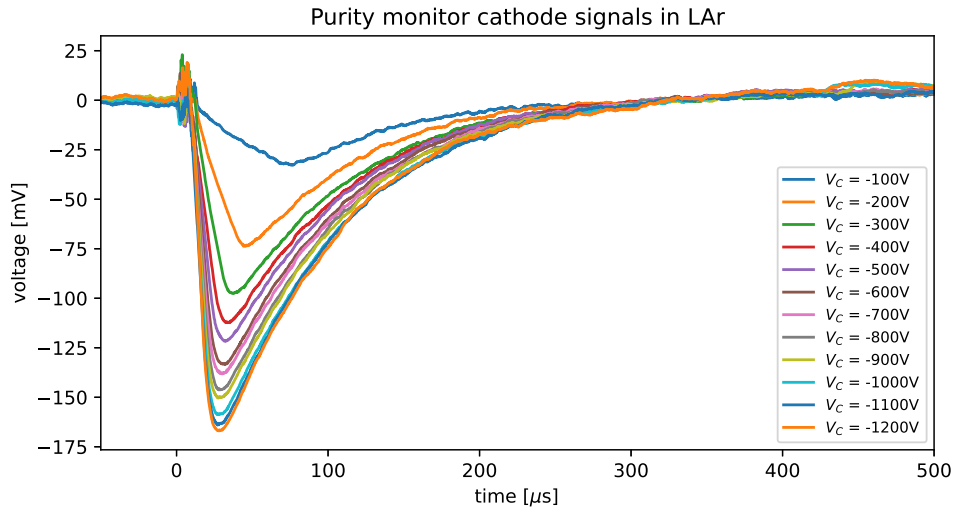


Figure 5.12: Cathode signals observed with the second purity monitor in LAr. The signals have a timing resolution of $0.2\mu\text{s}$ and are smoothed with a rolling average using a 15 point window.

We observed that the cathode signal amplitude increases as a function of cathode voltage. This was also an observation we made in gaseous argon and an observation made by Manenti et al. [16] in LAr. We also observed that the signal peak time decreases as a function of cathode voltage. The signal peak voltages and times are plotted in Figure 5.13 as a function of cathode field.

The peak amplitude V_{peak} and peak time t_{peak} are described well by exponentials. The exponential fit parameters are shown in Figure 5.13. The decreasing t_{peak} might be explained by the electrons taking less and less time to pass between the cathode and cathode grid as E_1 is increased. During the time the electrons are between the cathode and cathode grid, they can induce a current on the cathode which increases the peak voltage. If that time is shortened, then the time over which the charge amplifiers integrate the input current is shortened. The effective work function lowering

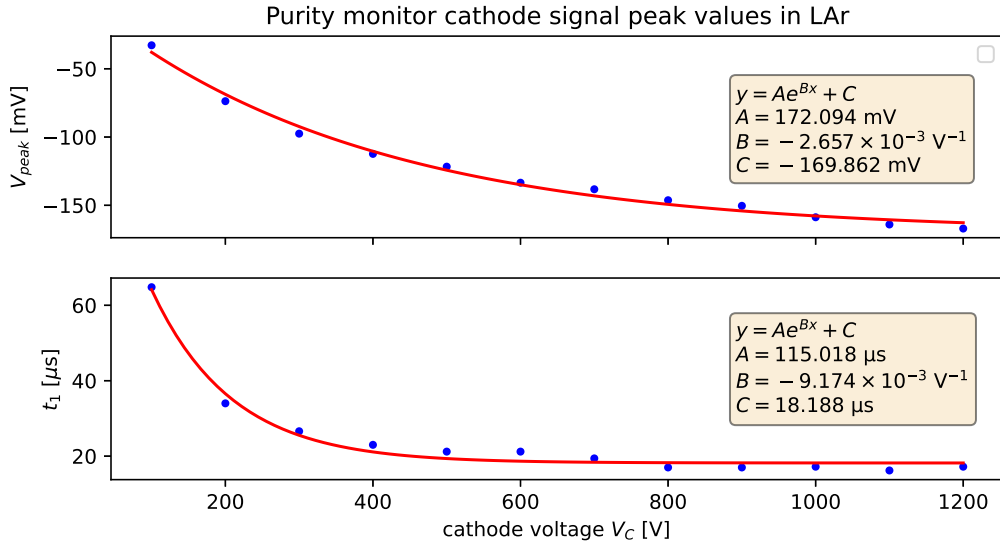


Figure 5.13: Cathode signal amplitude V_{peak} and peak time t_{peak} extracted from Figure 5.12 using the minimum data point after smoothing. Exponential fits are displayed in red with parameters shown.

as the field magnitude increases might explain why the signal amplitude increases. However, the effective work function decreasing only increases Q_C and does not change how long they take to pass the cathode grid. The decreasing time over which the induced current is applied due to the faster drift speed best explains the change in t_1 .

5.5.3 RC Correction for LAr Signals

As discussed in Chapter 2, current passing through the charge amplifier leads to a lowering of V_{peak} due to some current “leaking” through the resistor. If we just calculated CV_{peak} to calculate the charge, Q , the leakage charge due to this resistor is unaccounted for. This can be corrected for by using equation 2.6. If t_1 and t_3 were equal, and if the RC constant for each charge amplifier were equal, then these corrections would inevitably cancel out when calculating Q_A/Q_C and so they could be ignored. We cannot ignore this correction because t_1 does not equal t_3 since $E_3 > E_1$ and $d_3 < d_1$. Even if these times were equal, the two charge amplifiers have different values for R and C and so the correction cannot be ignored even in this case. Figure 5.14 shows the total charge, Q , the total leakage charge, Q_{leak} , and the peak charge, Q_{peak} , for each signal in Figure 5.13.

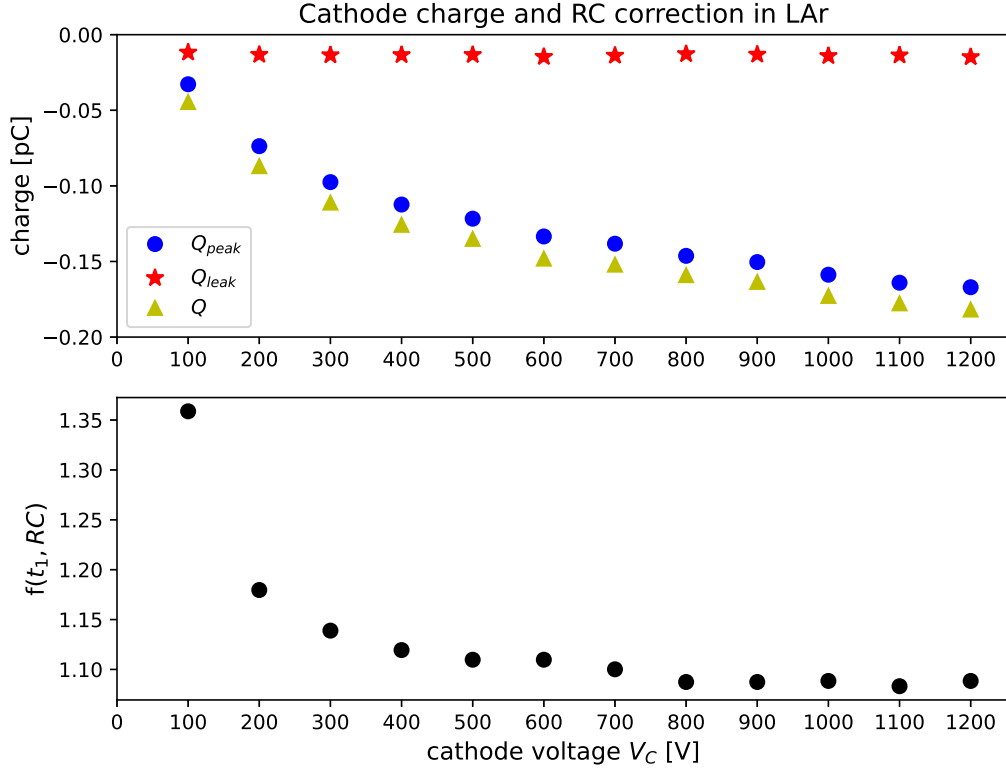


Figure 5.14: Calculated charge from the cathode signals from Figure 5.13. Q_{leak} is calculated using the RC correction in equation 2.6.

So we have

$$\begin{aligned}
 Q &= Q_{peak} f(t_1, RC) \\
 &= CV_{peak} f(t_1, RC)
 \end{aligned}
 \tag{5.1}$$

and

$$\begin{aligned}
 Q_{leak} &= Q - CV_{peak} \\
 &= CV_{peak} (f(t_1, RC) - 1)
 \end{aligned}
 \tag{5.2}$$

where

$$f(t_1, RC) = \frac{t_1/RC}{1 - e^{-t_1/RC}} \quad (5.3)$$

We see in Figure 5.14 that Q_{leak} remains fairly constant over the cathode voltages tested, while $|Q_{\text{peak}}|$ increases with V_C . It is not a surprise that $|Q_{\text{peak}}|$ increases since we have just multiplied V_{peak} by C and separated out the different components of Q . What is very interesting is that the correction factor, $f(t_1, RC)$, which is also shown in Figure 5.14, is anywhere between 1.08 and 1.36 in this V_C range. The reason for this is that while Q_{leak} is a somewhat small fraction of the total charge at $V_C = -1200V$ (8.1%), it is a substantially larger fraction at $V_C = -100V$ (26.4%). For normal running, which may be between $V_C = -100V$ and $V_C = -300V$, this correction is at least a 14% effect. This leads us to conclude that this correction should not be ignored when calculating electron lifetime.

5.5.4 Lessons Learned

No anode signals were observed in the first LAr run. Sparking occurred at about $V_A = 1300V$, just like what was observed in gaseous argon tests. The sparking set a strict limitation on the voltages we could use during this test. Our goal was to increase the cathode voltage as much as possible to increase the cathode signal size, which correspondingly increases the anode signal size. And also, the field ratio requirements of the purity monitor mean that if the cathode voltage is increased, then the anode voltage has to be increased proportionally. However, the sparking phenomenon meant the maximum operating voltages were about $V_C = 50V$ and $V_A = 1250V$. No anode signals were observed at the maximum operating voltages, and the cathode signal size was relatively small. It was clear that we needed to increase the voltages further to have a chance of seeing anode signals.

Before the second run, we moved the anode cryostat connection to a separate HV feedthrough that supported only one HV input. All the HV wires were replaced with fresh wires that support over 5kV. Sparking was not observed in gaseous argon prior to the LAr fill, and tests in LAr confirmed no sparking at least up to about 3.3kV. A new issue was noticed when running with voltages greater than about 1000V. Random signals that mimicked purity monitor signals could be observed on the oscilloscope readout. The frequency of these signals increased when the anode voltage was increased, and would become more sporadic. The presence of this noise made it very difficult and sometimes impossible to observe purity monitor signals. Therefore, this set a new limitation on the voltages we could use during this test. We concluded that the issue was the HV filter box, since this noise would occur even when the anode and cathode HV were not connected to the purity monitor. We were concerned that our HV filter box would not be able to handle these higher voltages we chose to run at. Eventually, one of the blocking capacitors failed at about 3.4kV. The next step is to redesign the HV filters to support running at higher voltages. We have also changed the anode to anode-grid resistance from $125M\Omega$ and to $150M\Omega$. This increases E_3/E_2 and makes it so this ratio satisfies the requirements for anode grid transparency. This requirement not being satisfied may have reduced the anode signal size by some amount.

5.5.5 Estimated Anode Signal Size

In the two runs of the new purity monitor design in LAr, we were unable to see any anode signals. The primary reason for this could be low LAr purity. In the last test of the SingleCube detector in LAr, we observed an electron lifetime of about 2-3 μs . The setup when testing the SingleCube detector in LAr was very similar to the setup used for testing the purity monitor in LAr. They used different LAr batches and the LAr was filtered. Even though we have not seen anode signals in the purity monitor, we can still estimate how large they would be at various values for electron lifetime. This will allow us to not only determine which electron lifetimes the purity monitor can measure, but also make a conclusion about if measuring an electron lifetime of 2-3 μs is feasible. Figure 5.15 shows a plot of electron lifetime versus estimated anode V_{peak} for the new purity monitor design. In the following plots, a factor of 1.05 is applied to all resistances due to cryogenic operation. Additionally, the cathode V_{peak} is multiplied by $f(t_1, RC)$ using t_1 extracted from the fit in Figure 5.13 and $RC = 100\mu\text{s}$. Then the estimated anode V_{peak} is divided by $f(t_3, RC)$ to recover the actual voltage that would be observed, where t_3 is calculated from the geometry since the actual t_3 is not known.

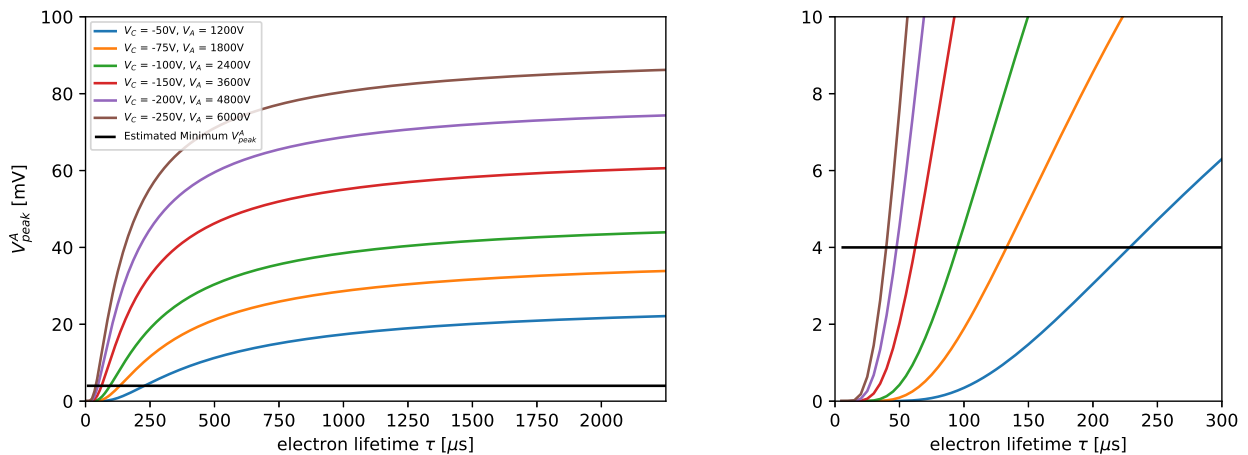


Figure 5.15: Electron lifetime vs estimated anode V_{peak} for the CSU purity monitor (14.2 cm grid to grid distance). The plot on the right is a zoomed in version of the plot on the left. The anode-grid to anode resistance is $125\text{M}\Omega$.

To make the plots in Figure 5.15, we multiply a cathode V_{peak} by $e^{-t/\tau}$ to determine an anode V_{peak} . The cathode V_{peak} is determined, at a specific cathode voltage, using the fit from Figure 5.13. The drift time t equals $t_2 + (t_1 + t_3)/2$, where $t_i = d_i/v_i$ ($i = 1, 2, 3$), d_i is a drift distance, and v_i is an electron drift speed in LAr. The electron mobility is calculated using a global fit to data (lar.bnl.gov/properties/trans.html) and depends on the electric field. The python code used to make the following figures calculates all the voltage drops, electric fields, and electron mobilities in the three purity monitor regions. The electron mobility multiplied by the electric field yields the drift speed. The voltages are set such that $E_2/E_1 \approx 2.6$. The black horizontal line in Figure 5.15 is 4 mV and is the smallest cathode signal we were able to see in the LAr runs. We use this as an estimate of the smallest anode signal we could realistically measure at the noise level we had. We might be able to measure a smaller signal than 4 mV, but it may be more difficult.

In Figure 5.15, we see that at $V_C = -50V$ and $V_A = 1200V$ the minimum electron lifetime we would be sensitive to is about $228 \mu\text{s}$. Another step up, at $V_C = -75V$ and $V_A = 1800V$, the minimum electron lifetime is about $133 \mu\text{s}$. Then at $V_C = -100V$ and $V_A = 2400V$, it is $95 \mu\text{s}$. Even at the highest voltage setting shown at $V_C = -250V$ and $V_A = 6000V$, it is $40 \mu\text{s}$. However, this anode voltage setting, and few of the other high settings in Figure 5.15 may not be accessible with our setup for the next tests in LAr. It is clear that even at very high voltage settings, a 2-3 μs electron lifetime could not be measured. While it is a good sign that electron lifetimes less than a few hundred microseconds could be measured with this setup, it is at the cost of needing fairly high anode voltages. It is important that we do not rely on being able to reach stable voltage levels this high, since our setup may not allow it. Thankfully, shortening the purity monitor decreases the anode voltage requirement. This is because if the drift length, d_2 , in the purity monitor is shortened, we would be applying nearly the same potential difference across a shorter distance. This way we would get the same drift field, as we would have in the longer version, but at a lower anode voltage. Figure 5.16 shows the electron lifetime versus anode V_{peak} for a purity monitor shortened to 7.47 cm full drift length (from 17.6 cm). The cathode-grid to cathode and anode-grid to anode distances are unchanged.

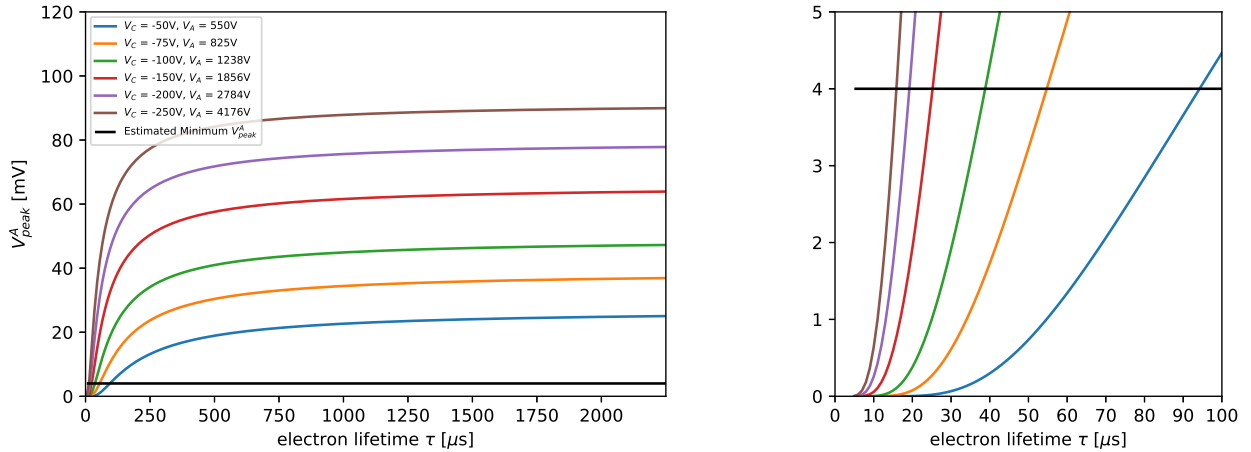


Figure 5.16: Electron lifetime vs estimated anode V_{peak} for the CSU purity monitor (4.39 cm grid to grid distance). The plot on the right is a zoomed in version of the plot on the left. The anode-grid to anode resistance is 150M Ω .

The first thing to note about Figure 5.16 is that the requirement on V_A is much lower now. Using the same values for V_C as in Figure 5.15, the minimum V_A needed for grid transparency is about half what was required for the longer purity monitor. On top of this, the minimum measurable electron lifetime is lower for each value of V_C . For instance, for $V_C = -50V$, this went from 228 μs to 94 μs by shortening the purity monitor. At $V_C = -75V$, it goes from 133 μs to 55 μs . At $V_C = -100V$, it goes from 133 μs to 39 μs . At the highest voltage setting shown at $V_C = -250V$ and $V_A = 4176V$, the minimum electron lifetime is 16 μs . It is clear from this analysis that we would be able to measure much lower electron lifetimes by shortening the purity monitor. This change would enable measuring low electron lifetimes at anode voltages that are more likely to be manageable with our setup (1-2kV). However, 2-3 μs would still not be feasible to measure at this purity monitor length. Shortening the purity monitor further will decrease the minimum measurable electron lifetimes but still leaves 2-3 μs out of reach. Reducing the length even further is limited by the presence of the grids, so the fundamental purity monitor design would have to be changed. We are nearing the limits of what a purity monitor can realistically achieve with regards to low electron lifetimes.

We should not forget about another important aspect of Figures 5.15 and 5.16. As the electron lifetime increases, the anode V_{peak} increases and eventually flattens as a function of τ . This happens because less and less electrons get lost to impurities as τ is increased, so Q_A reaches a maximum. Crucially, as Q_A approaches a maximum, it approaches the value of Q_C . As Q_A and Q_C get closer in value, the uncertainties on these values become very large relative to the differences between them. What this means is that as the electron lifetime gets higher, it becomes harder and harder to measure it. The remedy to this problem is to increase the length of the purity monitor. This will increase the drift-electron attenuation and make Q_A and Q_C more different from each other thereby reducing the uncertainties on the electron lifetime calculation. We make note of this now because we have been focusing on making low electron lifetimes more easily measurable. By doing that, we make longer electron lifetimes harder to measure. With this in mind, our goal going forward should still be to increase the anode signal size to prove that we can make electron lifetime measurements. However, we may need to adjust the purity monitor length at some point in the future depending on what values of electron lifetime our setup can achieve.

5.5.6 Next Steps

There are a few key actions that we can take to improve the prospects of measuring electron lifetime in LAr with the purity monitor. One of those actions is to decrease the purity monitor length to decrease the minimum measurable electron lifetime. The second, which will be more difficult, is to develop HV filters that can support higher operating voltages in the purity monitor. Higher cathode and anode voltages make measuring low electron lifetimes an easier endeavor, so it is important that we maximize the voltages we can achieve in our setup. Additionally, there will likely be changes to our LAr purification system before the purity monitor is tested in LAr again. These changes may involve either upgrading our LAr filters to be more efficient or implementing a way to recirculate the LAr through the filters. The latter would allow us to filter a batch of LAr multiple times until desirable purity is achieved. These changes will likely result in higher electron lifetimes which will make measuring purity with the purity monitor easier.

Chapter 6

Conclusion

Our primary goal has been to develop a purity monitoring system that can effectively measure electron lifetime in LAr. We developed a new purity monitor, designed charge amplifiers for use in our setup, and performed a variety of tests to assess the performance of the system. Tests of the first purity monitor design showed that signals could not be measured. The conclusion, which was informed by tests of the second purity monitor, was that the signals were likely too small to measure. Therefore, we were motivated to increase the size of the signals produced in the purity monitor. We applied methods to increase signal size, the most promising of which was upgrading the xenon flash lamp and using a silver photo-cathode. Initial tests of lenses also showed improvements in signal amplitudes for gold and silver in vacuum and gaseous argon, but a followup test is needed to determine their effectiveness in LAr.

Tests of our purity monitor design in LAr demonstrated that our system can produce large cathode signals. The cathode peak amplitude was shown to increase with increasing cathode voltage and, as a result, the anode signals will be larger as well. This means that higher applied voltages provide a higher S/N that helps to make a LAr purity measurement more easily extracted. The two recent tests of our purity monitor system in LAr uncovered issues that limited the applied voltages we could use and made it difficult to see anode signals above the noise. We solved the sparking issue but our tests also informed us that our HV filters need to be upgraded. We have shown that shortening the purity monitor is useful because it makes measuring smaller electron lifetimes easier. Overall, we have been able to make the purity monitoring system more mature and closer to being able to successfully measure LAr purity. Successful measurements of LAr purity with this setup means that the purity monitor will be a tool that can be used to support the operation of the SingleCube detector at CSU for future tests.

Bibliography

- [1] P Cennini, JP Revol, C Rubbia, F Sergiampietri, A Bueno, M Campanelli, P Goudsmit, A Rubbia, L Periale, S Suzuki, et al. Detection of scintillation light in coincidence with ionizing tracks in a liquid argon time projection chamber. *Nuclear Instruments and Methods in Physics Research Section A: Accelerators, Spectrometers, Detectors and Associated Equipment*, 432(2-3):240–248, 1999.
- [2] DUNE collaboration et al. Deep underground neutrino experiment (dune): Far detector technical design report. volume i. introduction to dune. *Journal of Instrumentation*, 15(8), 2020.
- [3] Daniel A Dwyer, M Garcia-Sciveres, D Gnani, C Grace, S Kohn, M Kramer, A Krieger, CJ Lin, Kam Biu Luk, P Madigan, et al. Larpix: Demonstration of low-power 3d pixelated charge readout for liquid argon time projection chambers. *Journal of Instrumentation*, 13(10):P10007, 2018.
- [4] T Doke. Fundamental properties of liquid argon, krypton and xenon as radiation detector media. In *Experimental Techniques in High-Energy Nuclear and Particle Physics*, pages 537–577. World Scientific, 1991.
- [5] Shinzou Kubota, A Nakamoto, Tan Takahashi, T Hamada, Eido Shibamura, Mitsuhiro Miyajima, Kimiaki Masuda, and Tadayoshi Doke. Recombination luminescence in liquid argon and in liquid xenon. *Physical Review B*, 17(6):2762, 1978.
- [6] Shinzou Kubota, A Nakamoto, Tan Takahashi, T Hamada, Eido Shibamura, Mitsuhiro Miyajima, Kimiaki Masuda, and Tadayoshi Doke. Recombination luminescence in liquid argon and in liquid xenon. *Physical Review B*, 17(6):2762, 1978.
- [7] Gabriela Araujo. Wavelength shifting and photon detection of scintillation light from liquid argon. 03 2019.

- [8] R Acciarri, M Antonello, B Baibussinov, M Baldo-Ceolin, P Benetti, F Calaprice, E Calligarich, M Cambiaghi, N Canci, F Carbonara, et al. Oxygen contamination in liquid argon: combined effects on ionization electron charge and scintillation light. *Journal of Instrumentation*, 5(05):P05003, 2010.
- [9] E Morikawa, R Reininger, P Gürtler, V Saile, and P Laporte. Argon, krypton, and xenon excimer luminescence: From the dilute gas to the condensed phase. *The Journal of chemical physics*, 91(3):1469–1477, 1989.
- [10] George Bakale and Werner F Schmidt. Effect of an electric field on electron attachment to sf6 in liquid ethane and propane. *Zeitschrift für Naturforschung A*, 36(8):802–806, 1981.
- [11] Steven D Biller, Daniel Kabat, Richard C Allen, Gerhard Bühler, and Peter J Doe. Effects of oxygen and nitrogen on drifting electrons in a liquid argon tpc. *Nuclear Instruments and Methods in Physics Research Section A: Accelerators, Spectrometers, Detectors and Associated Equipment*, 276(1-2):144–150, 1989.
- [12] W Hofmann, U Klein, M Schulz, J Spengler, and D Wegener. Production and transport of conduction electrons in a liquid argon ionization chamber. *Nuclear Instruments and Methods*, 135(1):151–156, 1976.
- [13] Y. Li, C. Bromberg, M. Diwan, S. Kettell, S. Martynenko, X. Qian, V. Paolone, J. Stewart, C. Thorn, and C. Zhang. Parameterization of electron attachment rate constants for impurities in LArTPC detectors. *Journal of Instrumentation*, 17(11):T11007, nov 2022.
- [14] Fulvio Mauri. Icarus: A second-generation proton decay experiment and neutrino observatory at the gran sasso laboratory. In Hans Volker Klapdor-Kleingrothaus, editor, *Beyond the Desert 2003*, pages 941–948, Berlin, Heidelberg, 2004. Springer Berlin Heidelberg.
- [15] B Rebel, M Adamowski, W Jaskierny, H Jostlein, C Kendziora, R Plunkett, S Pordes, R Schmitt, T Tope, and T Yang. Results from the fermilab materials test stand and status

- of the liquid argon purity demonstrator. In *Journal of Physics: Conference Series*, volume 308, page 012023. IOP Publishing, 2011.
- [16] Laura Manenti, Linda Cremonesi, Francesco Arneodo, Anastasia Basharina-Freshville, Mario Campanelli, Anna Holin, Ryan Nichol, and Ruben Saakyan. Performance of different photocathode materials in a liquid argon purity monitor. *Journal of Instrumentation*, 15(09):P09003, 2020.
- [17] Pax-10 pulsed xenon light source data sheet. *Excelitas Technologies*, 2011.
- [18] Platypus technologies, llc. <https://www.platypustech.com/gold-thin-films>. Accessed: 2022-08-05.
- [19] Angstrom engineering (substrata solutions). <https://substratasolutions.com/>. Accessed: 2022-08-05.
- [20] William M Haynes, David R Lide, and Thomas J Bruno. *CRC Handbook of Chemistry and Physics*. CRC Press, 2014.
- [21] O Bunemann, TE Cranshaw, and JA Harvey. Design of grid ionization chambers. *Canadian journal of research*, 27(5):191–206, 1949.
- [22] F. Hecht. New development in freefem++. *J. Numer. Math.*, 20(3-4):251–265, 2012.